

Accepted Manuscript

*Geological Society, London, Special Publications*

Current-controlled sedimentation in a megatransform system:  
a case study of the Charlie-Gibbs Fracture Zone

Evgenia V. Dorokhova, Sergey Yu. Sokolov, Ekaterina P. Ponomarenko, Leyla D. Bashirova, Tatiana L. Pugacheva, Zarina F. Urazmuratova, Daria N. Laskina & Kseniya O. Dobrolyubova

DOI: <https://doi.org/10.1144/SP553-2023-138>

To access the most recent version of this article, please click the DOI URL in the line above. When citing this article please include the above DOI.

Received 4 August 2023

Revised 8 May 2024

Accepted 9 July 2024

© 2024 The Author(s). Published by The Geological Society of London. All rights reserved. For permissions: <https://www.lyellcollection.org/permissions-policy>. Publishing disclaimer: <https://www.lyellcollection.org/publishing-ethics>

**Manuscript version: Accepted Manuscript**

This is a PDF of an unedited manuscript that has been accepted for publication. The manuscript will undergo copyediting, typesetting and correction before it is published in its final form. Please note that during the production process errors may be discovered which could affect the content, and all legal disclaimers that apply to the book series pertain.

Although reasonable efforts have been made to obtain all necessary permissions from third parties to include their copyrighted content within this article, their full citation and copyright line may not be present in this Accepted Manuscript version. Before using any content from this article, please refer to the Version of Record once published for full citation and copyright details, as permissions may be required.

## Current-controlled sedimentation in a megatransform system: a case study of the Charlie-Gibbs Fracture Zone

Evgenia V. Dorokhova<sup>1,2\*</sup>, Sergey Yu. Sokolov<sup>3</sup>, Ekaterina P. Ponomarenko<sup>1</sup>, Leyla D. Bashirova<sup>1,2</sup>, Tatiana L. Pugacheva<sup>1,2</sup>, Zarina F. Urazmuratova<sup>1</sup>, Daria N. Laskina<sup>1,2</sup>, Kseniya O. Dobrolyubova<sup>3</sup>

<sup>1</sup>Shirshov Institute of Oceanology, Russian Academy of Sciences, Moscow 117997, Russia

<sup>2</sup>Immanuel Kant Baltic Federal University, Kaliningrad 236041, Russia

<sup>3</sup>Geological Institute, Russian Academy of Sciences, Moscow 117997, Russia

ORCID ID: Evgenia V. Dorokhova, 0000-0002-0079-7342; Sergey Yu. Sokolov, 0000-0002-7197-852X; Ekaterina P. Ponomarenko, 0000-0002-0668-4226; Leyla D. Bashirova, 0000-0003-3083-0649; Kseniya O. Dobrolyubova, 0009-0007-1069-5175

Present addresses: ED, Shirshov Institute of Oceanology (Atlantic Branch), Russian Academy of Sciences, Kaliningrad 236022, Russia

\*Corresponding author (e-mail: zhdorokhova@gmail.com)

### Abstract

The Charlie-Gibbs Fracture Zone (CGFZ) is the main transform system in the North Atlantic Ocean. It serves as a primary deep-water gateway for the Iceland-Scotland Overflow Water (ISOW) current. Using high-resolution seismo-acoustic profiling, three types of contourite drift were identified in the valleys of the inactive fractures and active transform of the CGFZ: (1) channel-related drifts, (2) confined drift, and (3) plastered drift. The ISOW current is the main agent controlling drift formation in the northern valley and eastern part of the southern valley, while the Denmark Strait Overflow Water or Low Deep Water is suggested for the western part of the southern valley. Examination of two sediment cores shows that the contourite drifts at least at their upper parts consist of alternated muddy and silty contourites and pelagic/hemipelagic sediments. The contourite deposition corresponds to the present interglacial interval. During glacial interval (MIS 3-2) and the last glacial/interglacial transition, pelagic/hemipelagic sedimentation prevailed corresponding with high IRD input. The position of the highly productive Subarctic Front over the study area induced the formation of diatom ooze beds at the beginning of MIS 1 and high-carbonate pelagites during some intervals of MIS 3.

Marine transform faults and fracture zones occupy vast areas of the Earth's ocean floors and are conservative plate boundaries formed by strike-slip faults. Their morphology differs significantly from the surrounding abyssal plains and mid-ocean ridges, being narrow elongated depressions with steep walls (Hensen *et al.* 2019), meaning that they may serve as deep-water gateways through which water, sediments, and biota are exchanged with neighbouring plains (Hernández-Molina *et al.* 2008).

The Charlie-Gibbs Fracture Zone (CGFZ) is one of the main transform systems in the North Atlantic Ocean (Skolotnev *et al.* 2021b). Transform fault zones segmenting the axial part of the Mid-Atlantic Ridge (MAR) with an offset of ~300 km are rare. They are mainly concentrated in the equatorial and central sections of the Atlantic and were termed 'terminator faults' (Pushcharovskiy *et al.* 1995). Subsequently, these extensive structures, usually consisting of several transform troughs (Ligi *et al.* 2002), were termed 'megatransforms' (Skolotnev *et al.* 2020). In northern latitudes, the CGFZ is a unique structure.

The CGFZ is the primary gateway for the westward transport of Iceland-Scotland Overflow Water (ISOW) from the Iceland Basin to the Irminger Sea (Worthington and Volkmann 1965) (Figure 1). This water, formed during winter convection in the Nordic Seas and comprising part of a lower branch of the Atlantic Meridional Overturning Circulation system, is closely interconnected with global climate changes during the Quaternary Period (e.g., Broecker *et al.* 1985). The ISOW current has a significant sedimentological effect in the Iceland Basin, forming giant contourite drifts such as the Björn and Gardar drifts on the eastern flank of the Reykjanes Ridge (Bianchi and McCave 2000). Passing through the valleys of the CGFZ, the current may redistribute sediments due to increasing velocities, forming depositional and erosional morphological features. These processes occur in the deep-water gaps and gateways (e.g. Hernández-Molina *et al.* 2008; Glazkova *et al.* 2021) and fracture zones (e.g. Borisov *et al.* 2023). Sediments deposited under the influence of near-bottom currents represent valuable palaeoclimate archives (Rebesco *et al.* 2014). However, a profound understanding of the sedimentary processes is necessary to distinguish the climatic signals.

The CGFZ has received considerable attention from both tectonic and hydrological perspectives. The geology of the CGFZ has been extensively studied (Johnson 1967; Fleming *et al.* 1970; Olivet *et al.* 1974; Vogt and Johnson 1975; Lonsdale and Shor 1979; Searle 1979; Chernysheva and Kharin 2009; Skolotnev *et al.* 2021a), as has its seismicity (Lilwall and Kirk 1985; Aderhold and Abercrombie 2016) and seafloor topography (Skolotnev *et al.* 2021b). The hydrological regime has been investigated using oceanographic and mooring stations (Worthington and Volkmann 1965; Shor *et al.* 1980; Saunders 1994; Schott *et al.* 1999; Dobrolyubov *et al.* 2003; Bower and Furey 2017; Petit 2018; Gonçalves Neto *et al.* 2020), hydrological buoys (Morozov *et al.* 2010; Racapé *et al.* 2019; Zou *et al.* 2020), and modelling (Xu *et al.* 2018). Recently, interest in the CGFZ has increased due to the study of its benthic fauna (Priede *et al.* 2013; Keogh *et al.* 2022 and references therein), and parts of the CGFZ have been declared a Marine Protected Area (Smith and Jabour 2018).

Initial investigations of the depositional process focused on the near-bottom current direction, inferred from the sedimentation pattern in its valleys (Le Pichon *et al.* 1971a, b; Worthington and Wright 1971). More recently, it has been studied by side-scan sonar system and considerable thicknesses of sediment were registered in the active part of the northern transform valley (Searle 1981). Sedimentary characteristics have been considered locally (Shor *et al.* 1980; Faugères *et al.*

1983; Bashirova *et al.* 2017), and it was generally assumed that the main sedimentation drivers are the ISOW bottom current and turbidity currents. Owing to high sedimentation rates, sediments from the western part of the northern valley were used to reconstruct the ISOW regime during the Holocene (Kissel *et al.* 2009, 2013). However, details of sedimentation processes in the CGFZ remain poorly understood.

This study aims to reconstruct the sedimentary processes in the CGFZ during the Late Pleistocene to Holocene based on high-resolution seismo-acoustic profiling data and lithological studies of sediment cores.

### **Morphological and geological settings**

The CGFZ is located in the North Atlantic and offsets the axial part of the MAR at latitude  $\sim 52^{\circ}25'N$  by  $\sim 340$  km (Figure 1). It comprises two parallel transform valleys of an active offset part of the fault zone between the MAR spreading segments (Figure 2). Intra-transform domain (ITD) ridges separate the valleys and their summits have a depth of 2,000–3,000 m. A 40 km long intra-transform spreading centre connects the northern and southern transforms at  $\sim 31^{\circ}50'W$  (Figure 2). Active transforms occupy the two valleys from the spreading centre to the rift zones of the MAR, which we term the 'northern and southern active valleys' (Figure 2). Their inactive continuations are termed the 'northern and southern inactive valleys' (Figure 2). The depth of the northern valley varies from 3,500–4,860 m in the active section to 3,800 m in the inactive section, and the depth of the southern transform is up to 4,500 m and 3,900 m in its active and inactive sections, respectively. An outer ridge with a crest depth of 3,100 m bounds the northern inactive valley to the north (Figure 2). This ridge is a continuation of the small median ridge located at the intersection between the northern active valley and the intra-transform spreading centre (Skolotnev *et al.* 2021b). The tectonic and morphological characteristics of the CGFZ megatransform system are described in detail in Skolotnev *et al.* (2021b, a).

Megatransforms are of particular importance because they separate segments of the MAR with contrasting ages in the spreading processes starting in the Atlantic (Sokolov *et al.* 2020), and, consequently, the thermal evolution of the mantle over different durations. In particular, according to indexed magnetic anomalies (Müller *et al.* 2008), the MAR oceanic segment south of the CGFZ has a breakup age of between 130 and 108 Ma, while the segment north of the CGFZ has a breakup age of 59 Ma. This means that for a long period, parts of the CGFZ that are currently inactive represented the ocean-continent boundary of this transform type. The trigger for the opening of the MAR segment north of the CGFZ was the impact of the Iceland mantle plume (Dang *et al.* 2020); however, it is likely that this plume is not the main driving force causing the split and further drift of lithosphere plates (Storey 1995). The plume in the axial part of the MAR north of the CGFZ is limited by a cold structural barrier that prevents the flow of heated and partially molten mantle material southward over the CGFZ. This is confirmed by seismic tomography data (Schaeffer and Lebedev 2013) and a depth section along the MAR constructed from the SL2013sv model (Sokolov *et al.* 2022). This mantle-deep structure to the north and south of the CGFZ is also represented by the various compositions of magmatic rocks and, consequently, in the varying morphology of the ocean floor in the CGFZ and adjacent segments of the MAR (Skolotnev *et al.* 2021b). To the north of the CGFZ, the topography of the basaltic basement has features characteristic of highly productive magmatism, with volcanic edifices of the central type superimposed on the spreading ridge-like

relief and is hypsometrically more elevated than the southern segment. To the south of the CGFZ, the ridge-like relief becomes less pronounced, with an almost complete absence of volcanic edifices of the central type. According to existing data (Skolotnev *et al.* 2021b), the intra-transform area inside the CGFZ is composed of gabbro, dunites, and peridotites.

## **Oceanographic setting**

The CGFZ is one of the main corridors for surface to deep-water masses in the North Atlantic (Daniault *et al.* 2016). Surface water near the CGFZ represents a branch of the North Atlantic Current (NAC), which northern edge represents the Subarctic Front (SAF) (Saunders 1994; Daniault *et al.* 2016; Gonçalves Neto *et al.* 2020) (Figure 1). Together, the NAC and SAF serve as the transition zone between the waters of the subpolar (cool, fresh, and nutrient-rich) and of the subtropical (warmer, saltier and relatively nutrient-poor) gyres (Krauss 1986; Belkin *et al.* 2009; Bolton *et al.* 2018). In addition, oceanic fronts are known to be 'hot spots' of marine life due to increased primary production in the area of their influence (Belkin *et al.* 2009).

Intermediate depths (500–1,500 m) are occupied by Labrador Sea Water (LSW) propagating eastward through the CGFZ and carried by the NAC. The deep water is westward flowing ISOW, which exists at depths of 1,500–3,500 m (Daniault *et al.* 2016). The ISOW is formed by winter convection in the Nordic Seas and overflows to the Iceland Basin, spreading southward along the Reykjanes Ridge as a cold and dense contour current. It turns westward through the CGFZ and flows northward in the Irminger Sea along the western flank of the Reykjanes Ridge. In the Irminger Sea, the ISOW joins with the Denmark Strait Overflow Water (DSOW), which also originates in the Nordic Seas and descends southward along the Greenland margin at depths of 2,000–3,000 m, underlying the ISOW (Daniault *et al.* 2016). The ISOW and DSOW contribute to the formation of the North Atlantic Deep Water (NADW), representing the lower branch of the Atlantic Meridional Overturning Circulation (Figure 1). According to mooring observations, the ISOW is characterised by salinities greater than 34.94 and in situ temperatures from 2.4 to 3.4 °C (Bower and Furey 2017), which are elevated values compared to other deep-water masses in the region (e.g. Morozov *et al.* 2010).

Strongly modified Antarctic Bottom Water is another deep-water mass in the eastern North Atlantic that occupies depths of more than 4,000 m and is called the Lower Deep Water (LDW) at these latitudes (McCartney 1992; Daniault *et al.* 2016) (Figure 1). Despite there is little information on the distribution of the LDW in the western part of the North Atlantic Ocean, the presence of colder and fresher waters deeper than the ISOW in the valleys of the CGFZ has been reported by several authors, especially within the southern valley. However, the origin of these waters is unclear and they are variously referred to as NADW (Shor *et al.* 1980), DSOW (Dobrolyubov *et al.* 2003), or LDW (Bower and Furey 2017).

## **Material and methods**

### **Bathymetry and geophysical data**

Data used in this study includes multibeam bathymetry data, very high-resolution seismo-acoustic sub-bottom profiles obtained by the R/V Akademik Nikolaj Strakhov in 2020 (Skolotnev *et al.* 2021b, a), and two sediment cores obtained by the R/V Akademik Sergey Vavilov in 2021 (Skolotnev *et al.*

2023). A bathymetric chart with a resolution of 250 m was compiled based on a multibeam survey and other published data (Skolotnev *et al.* 2021b).

The seismo-acoustic profiles were obtained using an EdgeTech 3300 system. The system generates a modulated long signal with a frequency varying linearly between 2 and 6 kHz. The tapered waveform spectrum produces images with a virtually constant resolution with depth. A sound velocity of 1,600 m/s was used for the time-depth conversion. The maximum sub-bottom penetration was 60–80 m and the vertical resolution was 0.2–0.5 m. Some preliminary results were published by Skolotnev *et al.* (2021b, a). Additional archive low-resolution seismic profiles were used; namely V3012 and V2706, which were collected by a seismic profiler on the R/V Vema.

Echo types were differentiated using the classification of Damuth and Hayes (1977), Damuth (1980), and Kuhn and Weber (1993). Additional echo types were also distinguished in the study area based on the acoustic facies shown.

### **Sediment cores**

Two sediment cores (V53-C1 and V53-C2) were retrieved using a 6 m long gravity corer. Core V53-C1 (465 cm long) was recovered at a water depth of 3,851 m from the flanked terrace of the northern active valley. Core V53-C2 (520 cm long) was collected at a water depth of 3,138 m from the confined basin on the south-eastern slope of the Reykjanes Ridge (for details see Skolotnev *et al.* 2023). Earlier published data on sediment cores from the study area were also considered. The locations of all cores are shown in Figure 2 and Table 1. The sedimentary facies described in previous studies were reinterpreted for this study. The sediment cores were split onboard. One half was sampled at a 1 cm interval for further analyses, whereas the other half was used for lithological description and packed as the archive section.

*Micropaleontological analysis and IRD counts* were performed using 1 cm slice samples with a 40 cm step in the sediment fraction coarser than 100  $\mu\text{m}$ . Wet sediment samples were taken directly from the core using 8 cm<sup>3</sup> plastic cubes and washed in a sieve using distilled water. A minimum of 300 planktic foraminiferal shells were counted in each sample using a microscope. The percentage of *N. pachyderma* (sin.) was determined. The concentrations of IRD and total foraminiferal counts were calculated as numbers per 8 cm<sup>3</sup> of wet sediment. The volcanic glass grains were counted separately from quartz grains.

*Calcium carbonate content* of the sediments was determined by a coulometric method using an AN-7529M carbon analyser and 1 cm slice samples with 10 cm intervals.

*Chemical element composition* was obtained using a portable X-ray fluorescence analyser (Olympus Vanta-C) with 1 cm resolution in archive halves of the split cores. The  $\ln(\text{Ca}/\text{Fe})$ ,  $\text{Nb}/\text{Ti}$ , and  $\ln(\text{Si}/\text{Ti})$  ratios were used as proxies for the biogenic  $\text{CaCO}_3$ , and volcanogenic and biogenic silica components, respectively (Croudace and Rothwell 2015). The water content was retrieved from a ratio of Rayleigh to Compton peaks of argon X-rays following Boyle *et al.* (2015). The titanium concentrations were recalculated to the dry weight of the sample.

*Grain-size analysis* of the 1 cm sediment slices at 5 cm intervals was performed using a laser diffraction particle sizer (SALD-2300, Shimadzu) at the Immanuel Kant Baltic Federal University, Kaliningrad, Russia. The analysis was repeated twice for each sample: first for the bulk sediment and

then for the carbonate-free fraction following consecutive dissolution of organic matter by hydrogen peroxide and carbonates using hydrochloric acid following McCave *et al.* (1995b). The size distribution of the carbonates is represented by the difference in the size distribution of the bulk and carbonate-free sediment (McCave *et al.* 1995b).

Grain-size fractions were determined following the modified scale of Wentworth (1922). The boundaries between sand and silt and between silt and clay were 63  $\mu\text{m}$  and 4  $\mu\text{m}$ , respectively. The silt fraction was divided into sortable silt and fine-grained silt with a 10  $\mu\text{m}$  boundary as this value is significant for the dynamic behaviour of sediment (McCave *et al.* 1995b). The textural name of the sediment was given following the classification of Shepard (1954).

*Mineral composition* of the samples was analysed using X-ray powder diffraction at the Analytical Laboratory of the Institute of Oceanology, Russian Academy of Sciences, using an X-ray diffractometer D8 ADVANCE (Bruker AXS), with Cu-K $\alpha$ , Ni 0.02 filter, 40 kV, 40 mA, and a LYNXEYE strip detector. Data were collected by scanning in a discrete regime with a step size of 0.02, a counting time of 8 s per step, in the range of 2.5–70°2 $\theta$  with rotation. The X-ray diffraction data were processed and deciphered using DIFFRAC.EVA software. Corundum numbers from the International Centre for Diffraction Data database were used for the quantitative analysis. In total, 21 samples of 1 cm slices were analysed for the two sediment cores.

*Magnetic susceptibility* was investigated to determine the relative content of magnetic minerals, reflecting the terrigenous contribution to the sediment composition (Rothwell and Croudace 2015). The Bartington MS3 system with surface sensor MS2E was used for the analysis of the archive core section halves with a 0.5 cm measurement interval.

*Lithological descriptions and sedimentary facies interpretation* were made following published literature (Stow and Piper 1984; Rebesco *et al.* 2014; Stow and Smillie 2020) using visual macroscopic analysis and analytical data. Macroscopic analysis included colour, texture, compositional descriptions, and sedimentary structure examination. The composition of each facies was examined using a microscope.

*Radiometric accelerator mass spectrometry (AMS) <sup>14</sup>C dating* of three samples was performed at the AMS Golden Valley (Centre for Collective Use of Scientific Equipment 'Accelerator Mass Spectrometry', Novosibirsk State University and Novosibirsk Scientific Centre, Novosibirsk, Russia). The bulk planktic foraminiferal community was chosen for dating as carbonate shells were not found in sufficient amounts. The <sup>14</sup>C age was calibrated using Calib 8.20 software and MARINE20 calibration curve (Heaton *et al.* 2020) with a global ocean age ( $\Delta R$ ) of 550 years. The calibrated age is represented as cal ka BP (before present; the zero year is 1950).

*Age model* for the upper sections of the sediment cores was compiled based on linear interpolation between AMS <sup>14</sup>C dates and zero age on the horizon of 0 cm. The calcium carbonate (CaCO<sub>3</sub>), ice-rafted debris (IRD), relative abundance of the cold-water species *Neogloboquadrina pachyderma* (sin.), and total foraminiferal counts in the sediment cores were used for stratigraphic dissection of the lower undated core sections. Following the previous studies, the decrease in CaCO<sub>3</sub> content, together with an increase in IRD and *N. pachyderma* (sin.), were correlated with the cold intervals of the glacial cycle (McIntyre *et al.* 1972; Ruddiman and McIntyre 1976; Helmke and Bauch 2001). In

the V53-C2 sediment core, an additional time reference point was represented by the identified ash layer.

## Results

### Morphologies and echo types

The tectonic, erosional, and depositional features were distinguished using the bathymetric and echo type characteristics of the area. The erosional and depositional features are mainly confined to the valleys of the CGFZ. Therefore, these features were primarily considered when assessing the sedimentation processes in these areas. The description of the morphological features and corresponding echo types is presented separately to the valleys of the CGFZ to the east and west of the intra-transform spreading centre so the area is divided into the 'eastern and western sectors'. The eastern flank of the Reykjanes Ridge is also considered.

Fifteen echo types were identified in the area, which were combined into six groups (Figure 3). The layered (L) echo type is represented by continuous, distinct echoes with flat (L1, L4, and L5) or waved (L2 and L3) seafloor and continuous, sharp, parallel sub-bottoms. The high-amplitude (HA) echo type has been recognised locally as distinct continuous echoes with a thick (up to 11 m) high-amplitude and continuous or discontinuous internal reflections. Groups of hyperbolic (H) echoes correspond to often indistinct surface echoes with irregular (H1, H3, and H4) and regular (H2) overlapping hyperbolae. Discontinuous sub-bottoms are represented in the H1, H2, and H3 types. Acoustically semi-opaque patterns with chaotic reflections were assigned to the chaotic (C) echo types. C1 is typically seen as an acoustically transparent lens-shaped or horizontally stretched unit and C2 has very indistinct discontinuous echoes, both on the bottom surface and internally. Prolonged (P) echo types have high-reflective surfaces and are characterised by absent (P1) or irregular (P2) sub-bottoms. The irregular (I) echo type is represented by discontinuous and slightly undulating surface reflections with intermittent sub-bottoms. The distribution of the echo types is shown in Figure 4.

*Eastern sector of the CGFZ valleys.* The eastern sector is represented by a northern inactive valley and a southern active valley with its eastward inactive continuation (Figure 5a). The northern inactive valley is bounded by an outer ridge from the north and ITD ridges from the south (Figure 5a). The valley depths vary from 3,800 m to 3,900 m, with a weak inclination to the west. A moat was observed along the southern wall of the valley (Figure 5b–e). The width of the moat is 1,500–3,500 m and it is up to 20 m deep. In the western part of the valley, a smaller moat appears along the northern wall (Figure 5b). The moats are represented by L5 echo types (Figure 5a–c). A sheeted and mounded small-scale sediment drift joins the moat from the north in the central and eastern parts of the valley and is confined between two moats in its western part. The drift is characterised by stratified echo types (L1 and L2) (Figure 5a, d, and e).

The high-amplitude conformable sub-bottom reflection separates two acoustically semi-transparent intervals inside the drift at a depth of ~4 m below the seafloor (Figure 5d and e). The upper interval is well traced along the valley and was designated to seismic unit U1. In the northern inactive valley, this seismic unit is uniform but may demonstrate slightly different thickness and transparency in other valleys. The upper boundary of U1 is characterised by high-amplitude seafloor reflection and the basal boundary represents the erosional surface. Reflection terminations demonstrate downlap at the foot of the southern wall of the valley (Figure 5e) and end abruptly along the high-angle slope



of the northern wall (Figure 5d). Lower seismic units are mostly stratified but still have different acoustic characteristics such as within the northern inactive valley and in other valleys. Therefore, only the upper uniform unit U1 was identified in the study area. The second acoustically semi-transparent interval beneath the erosional surface is characterised by an even greater transparency and thickness (up to 7 m) than U1 (Figure 5e). This unit has a discontinuous basal boundary that becomes poorly visible at the base of the valley walls. The seafloor between the valley walls and moats is mainly represented by the C1 echo type (Figure 5a and e).

The bathymetry data revealed small-scale sediment waves (dunes) on the valley floor (Figure 5b and c). The wavelength of the dunes varies from 500–2,000 m and the wave height is 3–10 m. The dunes forms involute irregularities on the valley floor and were indistinguishable on the echo-sounding profiles due to their low vertical resolution.

The inactive fracture of the southern valley has depths of 3,600–3,800 m and its morphology differs in its eastern and western sections (Figure 5f). The eastern section is relatively flat and covered by sediment dunes. The western section has a rough bottom formed by flanks of the structural heights of the MAR. The archive seismic profile V2706 clearly shows an acoustically transparent sediment body in the eastern section of the valley (Figure 5g). A V-shaped channel joins the sediment body from the north. The channel is filled by acoustically stratified sediments with reflections onlapping onto the structural high of the ITD and the sediment body.

The depths of the southern active valley varies from 4,100–4,540 m (Figure 5a). It is the narrowest valley in the area. The valley bottom is complicated by an asymmetric median ridge 100–300 m high. Very low amplitude hyperbolae and scattered reflections (H4) were recorded here, indicating an absence of sediment.

*Western sector of the CGFZ valleys.* The western sector includes the northern active valley, its western inactive continuation, and the southern inactive valley. The northern active valley is typically deeper than 3,800 m, whereas its inactive continuation to the west is shallower and has a depth range of 3,600–3,750 m (Figure 6a). There is an east–west elongated basin with a maximum depth of 4,869 m in the eastern part of the northern active valley (Figure 6a). A sill with a depth of 3,800–4,000 m at 32°–32°20'W divides the nodal basin of the intra-transform spreading centre and the depression of the active transform. The sill is formed by the median ridge and northern slope of an oceanic core complex, developed near the intra-transform spreading centre (Skolotnev *et al.* 2021b). The C1, C2, and I echo types were found on the sill and in the elongated basin (Figure 6a and b). The western part of the valley deeper than 4,000 m is also characterised by non-stratified echo types (H3, I, P1, and P2).

There is an oblique terrace along the southern wall of the northern active valley (Figure 6a, c, and d). The terrace dips from west to east from a depth of 3,500–3,550 m to 4000 m, which coincides with a decrease in its height from 750–100 m. The horizontal part of the terrace is characterised by well-stratified sub-bottom reflections (L2) and the upper acoustically semi-transparent seismic unit was identified as U1 (Figure 6d and e). Archive low-resolution seismic profile V3012 shows that at least the eastern part of the terrace is built up by an acoustically transparent sediment body (Figure 6c). Sediment waves and dunes ranging 10–25 m high and 1–2 km in wavelength were found on the terrace and the sill. Sediment core V53-C1 was retrieved from the sediment wave crest in the central part of the terrace (Figure 6e).

The inactive continuation of the fault to the west, towards the limits of the study area, is generally U-shaped but is complicated by a terrace along the southern wall of the valley (Figure 6f). The terrace has a height of 70 m at the survey line and is represented by the stratified echo types L2 and L4. Along the terrace, there is a channel-like structure represented by an acoustically transparent upper interval (C1 echo type) approximately 6 m thick. This interval is bounded by a thick, high-amplitude first sub-bottom reflection and low-amplitude parallel reflections below, with onlapping reflection terminations (Figure 6f).

The southern inactive fracture valley has a depth of 3,800–4,000 m, which is the largest depth among the inactive fractures in the study area (Figure 6a). There is a low inclination of the seafloor toward the intra-transform spreading centre. Median ridges up to 150 m in height occur in the central part of the valley (Figure 6a, g, and h). Gently sloping sediment drifts with convex-up geometry were recorded between the northern wall of the valley and the median ridges (Figure 6g and h). The sediment drifts are bounded by moats, which are deeper along the southern slopes of the drifts. The depths of the moats in the sub-bottom profile locations are 5–15 m and the widths are 1,000–1,700 m. The widths of the bodies are 2,000–5,000 m, depending on the space between the median ridges and the ITD ridges. Thickening of the acoustically transparent intervals was observed at the crests of the bodies. The increasing acoustic signal penetration depth of ~70 m was recorded at the crest of eastern drift (Figure 6g). This drift is characterised by thick upper semi-transparent unit U1 (~9.6 m) and high-amplitude underlying reflections. The sediment drifts, tops, and low-angle slopes of the median ridges are represented by acoustically stratified echo types L1 and L2. The C1 echo type is widespread at the base of the valley walls and median ridges, and partly fills the channels (Figure 6g and h). Small-scale undulations 2–3 m high were identified on the top of the drift and sediment dunes of up to 10 m high cover the inner part of the valley. In the western drift, the first high-amplitude sub-bottom reflection becomes unusually thick and was attributed to specific echo type HA (Figure 6h).

*Reykjanes Ridge, ITD, and MAR.* In the study area, the Reykjanes Ridge is represented by the spreading segment and deepening sector of the eastern flank of the ridge, covered with sediments from the southern end of the Gardar Drift (Bianchi and McCave 2000). Well-distinguished sediment waves cover the seafloor to the east of 32.5°W (Figure 2 and Figure 5a). They have a latitudinal direction and are up to 20 m high and 2–3 km in wavelength. The sediment wave area is characterised by stratified echo types (L1–L4), whereas hyperbolic echoes are typical for high-angle slopes and ridge tops (Figure 5a).

The sub-bottom profile across a depression on the flank of the ridge, where the V53-C2 core was obtained and location of the Integrated Ocean Drilling Program (IODP) site 1304, showed pronounced features. A sediment drift with a U-shaped moat on its northern flank is located between the ridges at a depth of 3,100 m (Figure 7a and b). The depth of the moat is 55 m. The drift is characterised by parallel reflections (L1 echo type) and the thickness of the first sub-bottom transparent interval U1 is ~6 m. The acoustic reflections of the drift are aggradational in its horizontal part and progradational along the drift edge where the maximum penetration of the acoustic signal (~75 m) was found. The bottom of the moat is represented by the C1 echo type. The surface of the drift is covered in dunes 2–3 m high and 1.2 km in length (Figure 7c).

The intra-transform domain includes ridges, spreading centre, and nodal basins (Skolotnev *et al.* 2021b). The highest ridges (1,100–1,400 m in depth) are located at the flanks of the spreading centre. The western part of the ITD ridges is deeper than the eastern part, with ridge summit depths in the western part between 2,500 m and 3,000 m compared with 2,100–2,600 m in the eastern part. The troughs between the separate ITD ridges reach 3,500 m and 3,200 m in the western and eastern segments, respectively. The summits and high-angle slopes of the ridges are characterised by various hyperbolae and irregular and prolonged echo types (Figure 4, H1–4, P1, P2, and I). The nodal basins were not crossed by the echo-sounder profiler except at the northern part of the southern basin where the H2 echo type was found. Various hyperbolic echoes (H1, 3, and 4) characterise the spreading centre.

The western flank of the MAR adjacent to the southern valley comprises longitudinal ridges that deepen westward. Their depth varies from east to west from 2,100–3,400 m. Troughs deeper than 3,800 m occur in the western part. Sediment cover is absent on the MAR south of the southern active valley. Ridges are mainly represented by the H4 echo type, with H2 and C2 echo types in the rift valley (Figure 4). On the western flank of the MAR, south of the southern inactive valley, flat ridges and troughs between them correspond to layered (L1–4) and chaotic (C1) echo types, respectively.

### **Sedimentary facies**

Six sedimentary facies were identified in the two sediment cores (Figure 8 and Figure 9). Two facies are common in both cores (F1 and F2), whereas the F3–F6 facies are unique for each core.

*Facies 1 (F1) description.* This facies consists of clayey-silty and silty-clayey calcareous mud of grey to light greenish grey (V53-C1; 0–273 cm) and grey to olive grey (V53-C2; 0–318 cm) colour (Figure 8 and Figure 9). This facies is characterised by moderate bioturbation. Calcium carbonate content is greater than 33% in core V53-C1 and more than 30% in core V53-C2 and increases towards the core top in both cores. This trend is synchronous with the  $\ln(\text{Ca}/\text{Fe})$  ratio (Figure 8 and Figure 9). This facies is associated with a low percentage of *N. pachyderma* (sin), IRD counts, MS values, and  $\text{Ti}_d$  content (Figure 8 and Figure 9). The Nb/Ti ratio records low values and decreases to zero in the upper parts of the cores. The same slightly decreasing trend was found for the  $\ln(\text{Si}/\text{Ti})$  ratio.

The mean grain size of the bulk sediment varies from 2–13  $\mu\text{m}$  in core V53-C1 and up to 22  $\mu\text{m}$  in V53-C2 (Figure 10a and b). Following carbonate dissolution, the mean grain size decreases, with a maximum value of 8  $\mu\text{m}$  in V53-C1 and 10  $\mu\text{m}$  in V53-C2. Grain size distributions of the bulk samples vary from unimodal to polymodal, with well-pronounced peaks in the clay and very fine-grained silt fractions (Figure 10a and b). Component distributions show that the terrigenous fraction consists of clay to coarse-grained silt with a minimum size of 10  $\mu\text{m}$  on the grain-size curve. The biogenic (carbonate) fraction is mainly represented by very fine silt and clay sizes (Figure 10a and b). An exception is the upper horizons of the cores (4–5 cm, 20–30 cm, and 90–91 cm in V53-C1 and 50–150 cm in V53-C2) where a sand fraction (foraminiferal shells) is present.

The most abundant mineral is calcite, which varies from 55%–82% in core V53-C1 and from 69%–90% in core V53-C2, with larger values found at the tops of the cores (Figure 10a and b). The other principal minerals are clays, quartz, K-feldspars, plagioclase, and pyroxene in core V53-C1.

Amphibole (1–2%) and dolomite (1–2%) were detected only in the lower parts of the cores, at 187–188 cm and 264–265 cm in V53-C1 and 291–292 cm in V53-C2 (Figure 10a and b).

The F1 facies has a high CaCO<sub>3</sub> content, which is concentrated mostly in the clay, fine silt, and fine sand fractions and disguised the terrigenous component grain-size distributions (Figure 10a and b). Grain-size analysis following the removal of carbonate material enabled the detection of gradational trends in the terrigenous sediment. These trends are more visible in core V53-C2. Based on these changes in the grain-size composition of the carbonate-free sediment, F1 was divided into two facies: F1a and F1b. The F1a facies is characterised by a higher content of the mineral in the medium to coarse-grained silt fraction (up to 50%) compared with F1b, and a lower amount of the clay and fine to very fine-grained silt fractions (Figure 10a and b). In the F1b facies, the terrigenous medium to coarse-grained silt fraction content is approximately 30% in core V53-C2 and 20% in core V53-C1, with the remaining fractions represented by clay and very fine to fine-grained silt. The grain-size distributions of the carbonate-free sediment also differ in the F1a and F1b facies. The F1a facies is characterised by a pronounced mode in the medium to coarse-grained silt sizes (sortable silt), whereas in the F1b facies, this mode decreases and the clay to very fine-grained silt mode is more prominent (Figure 10a and b).

*F1 interpretation.* This facies is interpreted as having formed mainly under the influence of bottom currents. The concomitant influence of pelagic settling of the carbonate material is reflected in high calcium carbonate content and increased  $\ln(\text{Ca}/\text{Fe})$  values indicating high sea-surface bioproductivity during this interval. The prevailing clay to very fine silt sizes in the carbonate material reflects its main nannoplankton (coccoliths) composition (Trentesaux *et al.* 2001). This biogenic material and extensive bioturbation disguise the bi-gradational sequence typical for the contourites. Nevertheless, it is evidenced from the grain-size data through changes in the medium to coarse silt fraction of the carbonate-free sediment (Figure 10a and b). The periodical increase of mineral fraction content and mean size, without changes in the terrigenous sediment source, is attributed to intervals of the intensification of the bottom current (Stow and Faugères 2008). This concurs with the statement that the medium to coarse silt sizes are sorted by bottom currents due to selective deposition (McCave *et al.* 1995b; McCave and Hall 2006). Based on the terrigenous grain-size composition, the F1a and F1b facies are identified as silty and muddy contourites, respectively.

*Facies 2 (F2) description.* This facies is represented by IRD-bearing silty sand of grey to greyish brown (V53-C1) and grey to olive grey (V53-C2) colour (Figure 8 and Figure 9). This facies comprises the lower sections of the cores, at three intervals in core V53-C1 (273–333 cm, 376–392 cm, and 418–444 cm) and two intervals in core V53-C2 (321–342 cm and 379–520 cm). Striking features of this facies are its low CaCO<sub>3</sub> content (< 33%), high IRD content, and high percentage of *N. pachyderma* (sin) (> 50% in total foraminiferal counts). These characteristics are also accompanied by an increase in MS values and  $Ti_d$  content. High Nb/Ti ratio values were also recorded, as well as a small increase in the  $\ln(\text{Si}/\text{Ti})$  ratio. Moderate bioturbation is also typical.

Mean grain size is significantly higher than in the F1 facies and varies from 5–75  $\mu\text{m}$  and 7–81  $\mu\text{m}$  in the bulk and carbonate-free sediment of core V53-C1, respectively (Figure 10a). In core V53-C2, the mean grain size is slightly finer and ranges from 4–51  $\mu\text{m}$  in the bulk sediment and 6–32  $\mu\text{m}$  in the carbonate-free sediment (Figure 10b). The high variability in mean size is mainly due to the carbonate fraction content as evidenced by the difference between the bulk and terrigenous

distributions (Figure 10). The grain-size distributions of the bulk sediments have a single mode in the sand fraction (e.g. 284–285 cm in core V53-C1; see Figure 10a) and are polymodal in samples of finer grain-size (e.g. 470–471 cm in core V53-C2; see Figure 10b). The component distributions indicate that the carbonate material is mostly sand-sized, and the terrigenous fraction is characterised by various sizes from clay to sand.

Mineralogical composition is characterised by significantly lower calcite (< 50%) and higher quartz content (24%–31% in core V53-C1 and 14%–23% in core V53-C2) than in the F1 facies. The other principal minerals are clays, K-feldspars, plagioclase, and pyroxene. In contrast, orthoclase is absent and amphibole and dolomite show their highest values (up to 6% and 4%, respectively).

*F2 interpretation.* The F2 facies is interpreted as hemipelagic sediment dominated by terrigenous components. The polymodal grain-size distributions with the prevalence of coarse-grained silts and fine to medium-grained sands are formed mainly by vertical settling with advection of far-travelled terrigenous material (Stow and Tabrez 1998). The evidence of slow hemipelagic deposition is supported by moderate bioturbation. The coarser particles have glacial origin, which is confirmed by high IRD counts with a predominance of terrigenous quartz and volcanogenic minerals (Figure 8, Figure 9, and Figure 10). The increased rates of ice-rafted deposition are typical for the glacial intervals in the North Atlantic (e.g. Ruddiman 1977).

*Facies 3 (F3) description.* This facies consists of IRD-bearing silty-sandy calcareous mud with grey to light brownish grey and greyish brown colour (Figure 8). It is present only in core V53-C1 at 392–417 cm and 445–464 cm. The main difference from the F2 facies is the high CaCO<sub>3</sub> content (33%–50%) that is comparable with the F1 facies. Fluctuations in the ln(Ca/Ti) ratio were recorded, which appears to be conditioned by bioturbation. The percentage of *N. pachyderma* (sin) is the same as in the F2 facies. The IRD content is also high and even higher than in the F2 facies, with a maximum value of 127,000 grains per 8 cm<sup>3</sup> at the base of the core (464 cm) (Figure 8). The MS and Ti<sub>d</sub> values are slightly lower than in the F2 facies, while the Nb/Ti ratio is at the same rate as in the F2 facies (Figure 8).

Mean grain size is also very similar to the F2 facies; however, a notable difference was found in the high presence of carbonate material, which concentrates in the fine-grained sand fraction (Figure 10a and b). The quartz and plagioclase contents are also high (17% and 12%, respectively), whereas clays, K-feldspars, amphibole, pyroxene, and dolomite contents do not exceed 4% each (Figure 10a and b).

*F3 interpretation.* The elevated Ca/Ti ratios and CaCO<sub>3</sub> content, together with the high content of terrigenous fraction of sandy sizes and high IRD counts, suggest a simultaneous increase of biogenic carbonate and terrigenous material input. This facies is fully bioturbated, indicating a slow uniform sedimentation without the influence of turbidity currents (Stow and Smillie 2020). The high CaCO<sub>3</sub> content in the sediment is mainly provided by planktic foraminifera, which is evidenced by the prevalence of the sand sizes in grain-size distributions of the carbonate fraction corresponded to the foraminifera shells (Trentesaux *et al.* 2001) and the domination of *N. pachyderma* (sin). The increased biogenic production on the sea surface may result from the presence of the SAF over the study area, which is characterised by elevated primary productivity common for oceanic fronts (Belkin *et al.* 2009). High IRD counts, abundance of quartz and presence of gravel suggest that terrigenous material is mainly delivered by icebergs (e.g. Bond *et al.* 1992). This material is not

sorted by bottom currents as reflected in polymodal grain-size distributions of carbonate-free clay and silt fractions without the prevalence of the sortable silt in fine-grained fraction (McCave and Hall 2006). The dominance of polar foraminiferal species *N. pachyderma* (sin) and high IRD content correspond to cold sea-surface conditions during sedimentation that are common for glacial intervals (McIntyre *et al.* 1972). Therefore, we propose that F3 facies is a high-carbonate pelagite with an admixture of hemipelagic IRD material formed under the influence of SAF during cold climatic conditions.

*Facies 4 (F4).* This facies is characterised by silty clay with a grey and greyish brown colour that gradually changes to greenish grey at the bottom of the section (Figure 8). This facies was found in core V53-C1 at 333–376 cm. It is characterised by distinct sedimentary structures such as parallel lamination in the lower part of the section (355–376 cm), wispy, convolute lamination in the middle part (345–355 cm), and rare micro-bioturbation in the upper part. The CaCO<sub>3</sub> content, together with the ln(Ca/Ti) ratio, demonstrates low values (8% CaCO<sub>3</sub>). This is accompanied by an almost complete absence of foraminiferal shells. The IRD content is also negligible, but the MS values show a sharp increase and are up to nine times larger than those in the F1–F3 facies. The Ti<sub>d</sub> values also increase, while the Nb/Ti ratio is at the same level as in the F2 facies and the ln(Si/Ti) shows an abrupt decrease caused by a high titanium content.

As the F4 facies is mainly terrigenous, the grain-size distributions of the bulk and carbonate-free fractions are similar (Figure 10a). The sediment consists of a well-sorted fine to coarse-grained silt fraction (60%; 10–63 μm) with slight normal grading in the sediment grain size (see arrow in Figure 10a). The carbonate fraction is present in the clay and very fine-grained silt fractions.

The mineral composition of this facies is unusual. Among the low calcite and increased quartz content, there is a notable absence of K-feldspar, amphibole, and dolomite, but an increased orthoclase and pyroxene content. In addition, only this facies contains ilmenite.

*F4 interpretation.* This facies is interpreted as a fine-grained turbidite as the main features of a thin (upper) turbidite sequence are a distinct parallel lamination and the absence of bioturbation (e.g., Stow and Smillie 2020). The absence of IRD material and foraminiferal shells in the lower part of the layer collectively indicate instantaneous deposition from the fine-grained portion of the turbidite flow (Stow and Smillie 2020). Increased magnetic susceptibility and titanium content, together with low CaCO<sub>3</sub> values, indicate a volcanogenic or siliclastic origin of the turbidite (e.g. Hunt *et al.* 2015). The weak trend in sediment coarseness in the upper part of the bed is attributed to mixing with overlying, more carbonate-rich F2 sediments through bioturbation.

*Facies 5 (F5) description.* This facies consists of siliceous ooze with an olive colour and is only found in core V53-C2 at 342–355 cm (Figure 9). Layers up to 3 cm thick are also found at 318–321 cm and 492–494 cm. According to visual examination, the facies comprises water-saturated sediment with a laminated structure. Well-preserved fish bones were found in the ooze at 350 cm. Microscope examination showed that 80% of the sediment consists of diatoms with radiolarians and sponge spicules also present. This facies is characterised by peak values of ln(Si/Ti), whereas other parameters have minimal values (Figure 9).

According to grain-size analysis, the sediment is represented by very fine-grained sand to silt (80%). The grain-size distributions are polymodal, with modes in the clay and very fine-grained silt, and a

broad peak in the coarse-grained silt fraction (Figure 10b). The carbonate material appears in the coarse-grained silt and fine-grained sand fractions. In terms of mineralogical composition, distinguishing features are the presence of pyrite and an absence of amphibole, pyroxene, and dolomite (Figure 10b).

*F5 interpretation.* This facies is almost entirely represented by biogenic silica material with the prevalence of diatoms identified through microscope observations. Peaks in  $\ln(\text{Si}/\text{Ti})$  values confirm high biogenic silica content (Croudace and Rothwell 2015) (Figure 9). The grain-size distributions in the carbonate-free fraction reflect diatom and radiolarian shells rather than terrigenous sediment (Figure 10b). High pyrite content indicates the mineralisation of increased quantities of buried organic matter (Berner 1982). The bed with a high concentration of diatoms request specific conditions for its formation. According to Bodén and Backman (1996) and Kemp *et al.* (1996), these sea-surface conditions include the presence of zones of increasing primary production corresponding to hydrographic fronts. Such conditions provide a concentration of diatoms in the form of mats on the sea surface, their death because of nutrient depletion due to high consumption rates and subsequent sinking to the seafloor with the formation of diatom oozes and mats (Bodén and Backman 1996; Kemp *et al.* 1996). According to Bodén and Backman (1996) in the North Atlantic, these specific settings may be achieved in the area of SAF, whose modern position is very close to the CGFZ (Figure 1). Therefore we interpret this facies as diatom ooze formed due to relatively fast pelagic settling from the highly productive zone of SAF.

*Facies 6 (F6) description.* This silty sand with a dark grey colour occurs exclusively in core V53-C2 at 355–379 cm (Figure 9). The F6 facies has the lowest  $\text{CaCO}_3$  content, which coincides with the lowest  $\ln(\text{Ca}/\text{Fe})$  value and decreased number of foraminifera shells. This facies is associated with the highest IRD counts, of which 50% are volcanic grains (Figure 9). Increased MS and  $\text{Ti}_d$  content values are also recorded, as well as a peak in the  $\ln(\text{Nb}/\text{Ti})$  ratio.

The grain-size distributions are unimodal, with a mode in the very fine-grained sand fraction (Figure 10b). The carbonate material consists of silt sizes. The mineralogical analysis was performed for one sample from the bottom part of the F6 facies and shows strong similarity with the mineral content of the F2 facies.

*F6 interpretation.* This facies is interpreted as a tephra bed due to the large number of volcanic glass grains, high magnetic susceptibility values, and peak Nb/Ti values. The high IRD counts reflect deposition of far-travelled volcanic ash from a subaerial eruption, rather than delivering of volcanoclastic material by the drifting ice and icebergs. The dominance of the well-sorted terrigenous fine-grained sand fraction in the grain-size distributions indicates a prevalence of single-sourced sediment material (Figure 10b). The tephra layer was also detected in a nearby core (JPC-13) (Hodell *et al.* 2010) and was attributed to the North Atlantic Ash Zone 1 (AZ1), consisting of several ash interbeds and related to the Vedde Ash layer (Younger Dryas), with an age of  $\sim 12.1$  cal ka BP (Hodell *et al.* 2010; Thornalley *et al.* 2011). Therefore, in core V53-C2, the tephra layer at 370 cm depth corresponds with the Vedde Ash layer and may serve as an additional dating tie point with an age of  $\sim 12.1$  cal ka BP.

### **Facies associations**

Some of the identified facies form vertically stacked facies associations (FA-A, FA-B, FA-C, FA-D, and FA-E), which are described below and presented in the Figure 11.

Facies association A (FA-A) is formed from interbedded facies F1a and F1b (Figure 11). This alternation was identified only on the base of the grain-size composition of the terrigenous sub-fraction and was undistinguished by visual logging. The transitions between the coarser-grained F1a and finer-grained F1b are very gradual and their alternations form bi-gradational sequences (Figure 10a and b). This facies association comprises the upper parts of both of the studied cores (Figure 10a and b) and ranges from 270 cm in core V53-C1 to 305 cm in core V53-C2.

Facies association B (FA-B) corresponds to gradation between F2 and F1, where the latter is represented by FA-A. The FA-B association has a single appearance in each sediment core and is characterised by gradual, bioturbated contact (Figure 11, Figure 8, and Figure 9). The thickness of this association is 330 cm in core V53-C1 and 320 cm in core V53-C2.

Facies association C (FA-C) consists of the stacking of the F5 and F2 facies (Figure 11). This facies association was found in the lower part of core V53-C2 (Figure 9) and is characterised by a sharp contact between facies without bioturbation. The total thickness of the two FA-C associations is 60 cm.

Facies association D (FA-D) comprises the F3 and F2 facies (Figure 11). It appears twice and exclusively within the lower part of core V53-C1. The contact between facies is gradual and bioturbated. The thickness of the two FA-D units is 90 cm (Figure 8).

Facies association E (FA-E) is represented by gradation from the F2 to F4 facies and then back to F2 facies (Figure 11). The contact between the F2 and F4 facies is sharp (erosional?) whereas the boundary between the F5 and F2 is gradational and micro-bioturbated. This association is present in the lower part of core V53-C1 and has a thickness of ~80 cm (Figure 8).

### Age model

Two AMS <sup>14</sup>C dates were obtained for the sediments of core V53-C1 and one in core V53-C2; all obtained dates fall within the Holocene interval (Table 2). In the V53-C1 sediment core, the beginning of the Holocene (11.7 ka, Walker *et al.* 2009) was established approximately at 270 cm as indicated by the decrease in the *N. pachyderma* (sin) relative abundance and IRD content (Figure 8). In the V53-C2 sediment core, the Holocene boundary was established at 340 cm based on the AMS <sup>14</sup>C date of 11.18 cal ka BP. Additionally, the level of the distinguished ash layer identified as Vedde Ash bed with the well-known date of 12.1 cal ka BP was used as a tie point (Figure 9). The MIS 2/1 boundary was established at 300 cm in core V53-C1 and 410 cm in core V53-C2, respectively (Figure 8, Figure 9). In the V53-C1 sediment core, the interval of high CaCO<sub>3</sub> content at 390-465 cm is assigned to MIS 3 suggesting the MIS 3/2 boundary at ~390 cm. The lower boundary of MIS 3 remains uncertain. According to constructed age model, we suggest that the V53-C1 core goes back to MIS 3 covering more than 50 kyr, whereas, the V53-C2 core goes back to MIS 2 covering more than 20 kyr. Average sedimentation rates for the dated intervals of the Holocene sediments are 20 cm/kyr in core V53-C1 for 0-161 cm and 24 cm/kyr in core V53-C2 for 0-320 cm.

### Discussion



## Morphological features and sedimentary processes

*Current-controlled sedimentation.* Examination of the multibeam bathymetry and echo-sounder data identified sediment bodies with a mounded and sheeted geometry and associated channels and moats in the valleys of the CGFZ and at the eastern flank of the Reykjanes Ridge. The sediment bodies and channels are covered by dunes and sediment waves. Their internal structures are characterised by stratified and undulating echo types. These distinctive morphological and seismic features reflect the uneven sedimentation processes in the valleys. Pelagic or hemipelagic sedimentation, typical for vast areas of the ocean, produces a uniform sediment cover over bottom irregularities (Moore 1969; Davies and Laughton 1972). Therefore, gravity-driven deposition or bottom-current activity may be responsible for the observed sediment distribution. Mass-transport and gravity flow deposits are well distinguished on high-frequency echograms, as they have diffuse, fuzzy, and acoustically transparent echoes (Damuth 1980), whereas layered echo types with continuous parallel reflections, corresponding to the stratified units, are common for contourite deposits (Kuhn and Weber 1993; Stoker *et al.* 1998; Faugères *et al.* 1999; Rebesco and Stow 2001). Therefore, based on the morphology and the distribution of echo types, we interpret the mounded and sheeted sediment bodies as contourite drifts and contourite channels and moats that formed under the influence of bottom currents. According to diagnostic criteria, summarised in Rebesco *et al.* (2014), channel-related, plastered and confined drift types have been inferred.

*Channel-related mounded and sheeted drifts* were identified in the northern and southern inactive fracture valleys. The channel morphology of the northern inactive valley is shaped by the ITD ridges and the outer ridge that form the southern and northern walls of the channel, respectively. The drift is located mainly along the northern wall and is characterised by mounded and sheeted morphologies and axial thickening of reflections (Figure 5d and e). Moats, located along the southern and northern walls, have a predominantly non-depositional, rather than erosional, character, which can be perceived from the condensing reflections and the absence of truncated terminations (García *et al.* 2009). The location of the moats on both sides of the drift is a common feature of this drift type (Rebesco *et al.* 2014; Esentia *et al.* 2018) and reflects an intensification of the current along the ITD ridges and the outer ridge. Due to the two-sided position of the erosive/non-depositional features, it is not possible to determine the direction of the bottom current, which could be bidirectional or recirculating in the restricted morphology of the valley (e.g. Morozov *et al.* 2010; Glazkova *et al.* 2022). A uniform visible sediment thickness in the moat and drift in the central part of the valley (Figure 5d) indicates that the present moat, at least in this location, may be inherited from previous asymmetric depositional or tectonic processes. The floor of the valley is covered in small, irregular sediment dunes common to areas of increased hydrodynamic activity (Stow *et al.* 2009). While cross-valley seismo-acoustic profiles are scarce, the bathymetric profiles show the asymmetry of deposition and the presence of the contourite drift along the entire northern inactive valley (Figure 5b and c).

Channel-related drift is also proposed in the eastern part of the southern inactive valley (Figure 5g). The position of the contourite channel along the northern edge of the drift is supposed to be conditioned by the presence of ITD ridges and/or the westward direction of the main near-bottom current. The small sediment dunes on the bottom surface and high-amplitude parallel reflections in the moat confirm an intensification of the current along the valley (Figure 5g).

The channel-related mounded drifts were also detected in the western section of the southern inactive fracture valley. The drifts are restricted by ITD ridges to the north and median ridges to the south (Figure 6a, g, and h). The median ridges are represented by tectonic piercement structures (Skolotnev *et al.* 2021b). Similar to the northern inactive valley, the drifts have mounded geometry with moats located along the northern and southern flanks. In the mounded part of these drifts, a divergence in reflections was found, and lapout terminations are associated with the moats that confirm uneven sedimentation under a bottom current control (Faugères *et al.* 1999). Sediment dunes are widespread on the seafloor, indicating the influence of a bottom current in the valley (Stow *et al.* 2009). Drifts were observed on two echo-sounder profiles; however, given the mounded geometry of the valley bottom, we infer that contourite drifts are more frequently distributed in the central part of the valley between 32°5'W and 34°W.

*Plastered drift* was identified in the northern active valley. In this valley, the most striking feature is the elongated basin of tectonic origin (Skolotnev *et al.* 2021b). The ubiquitous distribution of high-scattering C2 echo types at the bottom of the basin (Figure 6a) and the irregular and prolonged reflections (C2, P2, P1, H3, and I) in the transform trench further to the west (Figure 6a) indicate the absence of a thick sediment blanket. Conversely, the terrace at the southern wall is represented by acoustically transparent sediment drift adjusted to the ridges of the ITD, as shown in the low-frequency seismic profile V3012 (Figure 6c). The high-resolution seismo-acoustic signals penetrate the upper part of the sediment drift only, which is characterised by a slightly mounded shape and stratified acoustic structure (Figure 6a, d, and e). The presence of the contourite drift concurs with Searle (1981) who also reported a thick sediment body along the southern wall of the valley.

The origin of the drift is not entirely clear and could be partly due to tectonic processes. We suggest that the elongated basin and deep depression along the northern wall of the transform could have been developed through recent faulting along the terrace. High-magnitude earthquakes in this area and the pull-apart type of the elongated basin concur with this assumption (Aderhold and Abercrombie 2016). The absence of acoustically stratified sediments in the new tectonic depression supports the recent formation of the depression and the prevalence of gravity-driven depositional processes. The deep depression and elongated basin may serve as a corridor for the current favouring lateral sedimentation on the terrace. Based on the high-resolution seismo-acoustic profiling, the upper part of the plastered contourite drift is mostly aggradational; however, an upslope progradation at the northern edge of the drift is visible (Figure 6d), which probably corresponds to the interaction of bottom-currents with the drift morphology (Faugères *et al.* 1999). The total thickness of the drift sediments could not be determined due to the low penetration of the acoustic signal. Therefore, it is not clear whether drift deposition began before or after the faulting and whether there is a basement structure inside the drift. Regardless, at present, the northern slope of the drift is steep (up to 16°), which may be caused by faulting in this tectonically active valley.

A similar, but smaller scale, acoustic pattern and morphology were detected on the single transverse profile in the inactive western part of the northern valley (Figure 6f). A terrace is present along the southern wall of the valley. The upper part of the terrace comprises contourite drift, as indicated by its mounded geometry, layered echo types, and a sediment aggradation pattern at the northern edge of the terrace. Contrary to the active segment of the transform valley, the channel along the terrace is represented by a flat and convex-down stratified reflection pattern. This is suggestive of

the sediment infill of the channel resulting from gravity-flow deposits. The predominantly turbiditic composition of the nearby sediment cores KS 7911 and KS 7912 (Faugères et al. 1983) (Figure 4 and Figure 6f) confirms this hypothesis.

*Confined drift* was found in the isolated depression on the eastern flank of the Reykjanes Ridge. It is characterised by a mounded geometry with a moat along its northeastern slope (Figure 7). This moat separates the drift from the constraining ridges and is represented by the C1 echo type that may be interpreted as gravity flow deposits or channel-related sediments, formed under strong currents. The overall drift geometry is typical for mounded separated drifts (Faugères et al. 1999; Rebesco et al. 2014); however, drift dimensions are restricted by the surrounding ridges, meaning it can be defined as confined drift. The drift and moat positions suggest that the bottom current enters the depression from the northeast and propagates to the north and south along the structural highs (Figure 7a). Taking into account the position of the drift, it is considered to be a southern continuation of the Gardar Drift elongated on the eastern flank of the Reykjanes Ridge (Figure 1), (Bianchi and McCave 2000; Channell et al. 2006).

*Gravity flow deposits.* Debris flows and turbidity currents are common along the MAR due to rough relief and high seismic activity (e.g. Van Andel and Komar 1969; Mitchell 2018). In our study, following Damuth (1980), acoustically transparent or chaotic records with diffuse and prolonged surfaces and flat or hummocky relief are interpreted as mass transport and gravity flow deposits (Figure 3 and Figure 4). These deposits were detected locally at the base of the ridge slopes in the inactive part of the fracture zone (Figure 5e, Figure 6g, and h), on the eastern and western slopes and at the bottom of the elongated basin of the northern active transform (Figure 6a and d), and on the bottom of the western part of northern inactive fracture valley (Figure 6f). In the northern inactive valley, the acoustically transparent interval under the basal reflection of U1 may correspond with buried mass transport deposits (Figure 5d and e). In the southern inactive valley of the western sector, deposits of downslope density currents are frequent at the foot of the ITD ridges, the southern slope of the valley, and high-angle slopes of median ridges (Figure 6a, g, and h). Acoustically transparent lenses with onlap terminations fill the moats of the westernmost contourite drift in the southern inactive valley (Figure 6h), suggesting partial burying of the drift by turbidites (Faugères et al. 1999). At the base of the ridges, chaotic echo types imply the development of gravity processes when the sediment on the ridge slopes reaches unstable conditions. The high seismicity activity in the region, related mainly to the active transforms and rift valleys (Skolotnev et al. 2021b), triggers the gravity processes and promotes this wide distribution of gravity flows and mass transport deposits. The presence of turbidites and mass flow deposits in the valleys of the CGFZ was also registered in previously studied sediment cores (Faugères et al. 1983; Bashirova et al. 2017) (Figure 4).

#### **Bottom current variations and depositional environment reflected in sediment and acoustic data**

*Facies associations.* The grain-size composition of muddy and silty contourites of facies association FA-A indicates deposition under weak bottom currents (about 10 cm/s) (Figure 11). The fine-grained bi-gradational sequences of gradually altered finer F1b and coarse F1a facies resemble C1–C2 and C4–C5 divisions of the standard contourite sequence (Stow and Faugères 2008). The finer unit is deposited under very low or absent current control and may also reflect hemipelagic deposition (e.g. Stow and Faugères 2008; Yu et al. 2020). The coarser unit is typically settled from the suspended

load as the current intensity increases (Brackenridge *et al.* 2018). Such changes in the depositional regimes correspond with contourite drift accumulation under weak bottom currents distally to the current core (e.g. de Castro *et al.* 2021). The muddy and silty sizes of the contourites may also be explained by the prevalence of fine-grained material in the sediment source that can be distantly located or represented by resuspended particles and particles pirated by the bottom current from very low-density, fine-grained turbidity currents. The relatively high content of calcareous nanofossil material, unsorted by bottom currents, implies the influence of pelagic settling.

The FA-B association corresponds to the shift from hemipelagic facies to fine-grained contourites. This sequence differs from the FA-A association by the prevalence of IRD of fine to medium sand sizes in the hemipelagic sediment (facies F2). Poor sorting of IRD-bearing sediment and polymodal grain-size distributions suggest an absence of sorting by bottom currents. The FA-B sequence changed to FA-C and FA-D in the lower parts of the sediment cores; those comprising facies F5 and F3 were formed under pelagic settling of biogenic material derived from highly productive sea-surface areas (Figure 11). Intercalation of the hemipelagic and pelagic facies suggests that the bottom currents were inactive during this interval of sediment formation.

The FA-E association is interpreted as base-cut-out fine-grained turbidite, whose deposition interrupts the slow hemipelagic sedimentation (Figure 11). Such partial turbidite sequence could be deposited from the distal part of the turbidity current or represent an overbank deposit (Stow and Smillie 2020). Both processes are possible and agree with the position of core V53-C1 on the top of the sediment wave and to the east of the local depression on the terrace of the northern active valley (Figure 6e). This depression may serve as a channel for the axial part of gravity flows originating on ridges of the ITD and passing the terrace down to the bottom of the transform. The chaotic acoustic reflections (C1 echo-type) in the channel, interpreted as gravity flow deposits, support this assumption (Figure 6e).

Vertical stacking pattern of the facies associations expresses changing from mainly vertical settling processes in the lower parts of the sediment cores to current-controlled sedimentation in the upper sections. Contouritic and pelagic/hemipelagic sequences occupy the same intervals in both sediment cores, assuming a time dependence of the activity of the bottom current.

*Cyclic pattern of seismo-acoustic records.* The high-resolution seismo-acoustic profiles show a distinct alternation of more transparent units (T) with higher amplitude reflection packages (R). This pattern is well defined in the axial parts of the plastered and confined drifts in the northern active valley and eastern flank of the Reykjanes Ridge and is expressed as layered echo types (Figure 6d, e, and Figure 7b). The correlation of profiler and sediment cores data shows that the upper acoustically semi-transparent interval U1 corresponds with the fine-grained contourite association FA-A formed during the warm MIS 1 and characterised by high sedimentation rates (up to 24 cm/kyr) (Figure 12). The underlying high-amplitude reflections (R) correspond with the F2 facies and FA-D facies association accumulated during the cold MIS 3–2. We suppose that the high acoustic reflectivity of these sediments is caused by the high IRD content (i.e. sand material) in the F2 and F3 facies, which leads to lower porosity and amplified bulk density (e.g. Bond *et al.* 1992) that increase an acoustical impedance (Richardson and Briggs 1993). A comparison of the seismo-acoustic data with the 13JPC core (Hodell *et al.* 2010) confirms that the high-amplitude reflections coincide with glacial sediments with high IRD content (Figure 12). The reason for the different thicknesses of these reflections and,

consequently, of the glacial sediments at the V53-C2 and V53-C1 coring sites is unclear and requires further investigation. However, given the correlation of the seismo-acoustic and sediment core data, we suggest that the acoustically transparent units (T) may have formed under the influence of bottom currents during interglacials. In contrast, units with amplified reflections (R) correspond to hemipelagic/pelagic deposition with high IRD input and the absence of current control. Therefore, at least in their upper parts (~70 m), the sampled contourite drifts may consist of alternated contouritic and pelagic/hemipelagic sediments rather than pure contourites. These cyclic variations in lithology and seismo-acoustic patterns of the drifts are interpreted as due to variations in bottom current influence and sediment supply. This interpretation differs from the data on drifts formed in other sediment environments such as, for example, Faro Drift, where lithological and acoustical alternations were attributed to the bottom current intensity (Stow *et al.* 2002). We suppose that the intercalation of the contouritic and pelagic/hemipelagic sedimentation in the drifts due to variations of control by bottom current and sediment sources could be common for regions where both are strongly linked to climate changes, with examples from the North Atlantic contourite drifts (e.g. Cremer *et al.* 1993).

### **Water masses and contourite drifts: sedimentary model**

The valleys of the CGFZ are mainly filled with ISOW and its westward current was thought to be the main driver of current-influenced sedimentation (Shor *et al.* 1980; Searle 1981; Faugères *et al.* 1983). However, according to more recent hydrographic observations (e.g. Bower and Furey 2017), the depths of the axis (2,000–3,000 m) and lower boundary (3,500 m) of the ISOW are typically shallower than the valleys of the CGFZ (3,800–4,600 m). Therefore, a deeper water mass can be present in the valleys. Such a deeper, colder, and fresher water mass was repeatedly reported by oceanographic observations, especially in the southern valley (Shor *et al.* 1980; Saunders 1994; Dobrolyubov *et al.* 2003; Bower and Furey 2017). The origin of this water mass is contradictory, being variously interpreted as LDW (Bower and Furey 2017) or DSOW (Shor *et al.* 1980; Dobrolyubov *et al.* 2003). This water mass enters the valleys from the west (Saunders 1994; Daniault *et al.* 2016) and its direction is mainly eastward in the southern valley (Dobrolyubov *et al.* 2003; Bower and Furey 2017) but could be westward in the northern valley due to entrainment by the ISOW current (Shor *et al.* 1980). According to Shor *et al.* (1980), the fresher and denser near-bottom water mass (DSOW) may penetrate from the southern to the northern valley through depressions between the ridges of the ITD. The mean current speed of the westward-flowing ISOW is greater than 6 cm/s in the northern valley, whereas the mean current speed of the eastward-directed near-bottom water is approximately 2 cm/s in the southern valley (Bower and Furey 2017). The eastward transport may be enhanced due to deep intrusions of the eastward-flowing NAC over the CGFZ (Saunders 1994; Bower and Furey 2017; Xu *et al.* 2018; Racapé *et al.* 2019). Of note, most of the oceanographic measurements were carried out on a transect at 35°W, with the deepest measurement at approximately 3,700 m in the northern valley and 3,850 m in the southern valley that is shallower than the bottom of the valleys to the east of this transect.

As such, the following sedimentation model is proposed for the CGFZ area. The westward-directed ISOW current readily enters and fills the northern valley from the northeast (Figure 13). The depths of the eastern part of the ITD ridges (2,000–2,500 m) and intervening depressions (up to 3,350 m) enable the ISOW current to penetrate the eastern part of the southern valley. The constricted valleys intensify the near-bottom current, which is responsible for the erosional or non-depositional

elements along the ridges and drift accumulation at the areas of current decrease (Hernández-Molina *et al.* 2008). The ISOW current is responsible for the formation of the contourite drifts in the isolated depression on the eastern flank of the Reykjanes Ridge, in the northern valley, and eastern part of the southern inactive valley (Figure 13). The contourite drifts in the southern inactive valley (western part) are formed mainly under the influence of the deeper, eastward-flowing LDW (or DSOW), which enters both valleys from the east, but significantly, is blocked by the ISOW current in the northern active valley at the terrace depth of 3,500–4,000 m (Saunders 1994) (Figure 13). However, the fault depression at the northern edge of the terrace, with a maximum depth of 4,870 m, may be filled by this fresher and denser water mass, although this assumption requires additional hydrographical observations. The location of the drifts of the northern valley and the flank of Reykjanes Ridge deeper than the core of the ISOW current determines muddy and silty types of the contourites. This concurs with, for example, de Castro *et al.* (2021) who have shown that muddy and silty contourites are formed distal to the bottom current axis. The distal location of the plastered contourite drift is also confirmed by non-migratory sediment waves on the top of the drift that correspond to sluggish bottom current characteristics (Bianchi and McCave 2000; Faugères and Mulder 2011).

The sediment material of studied contourite drifts mainly comprises terrigenous and biogenic components with some addition of volcanogenic. The contouritic sedimentation is provided by the ISOW current, which delivers fine-grained terrigenous particles. The nepheloid layers within the ISOW were found on the eastern slope of the Reykjanes Ridge at depths of 2,200–2,500 m (Bianchi and McCave 2000) and in the western part of the northern valley (35°W) at depths of 2,000–3,200 m and 3,550–3,700 m (Shor *et al.* 1980). ISOW provides the detrital fraction gathering resuspended particles along the Gardar Drift and fine-grained material from turbidity currents at the head of the Maury Fan (Davies and Loughton 1972; Bianchi and McCave 2000; Kissel *et al.* 2009). This material originates from the Faroe Bank Channel and the Iceland-Faroe Ridge and consists mainly of basaltic grains from the Iceland Shelf and distal volcanic silts and fine sands (Ruddiman 1972). In the CGFZ area, these sediment particles may settle from the nepheloid layers and/or be redistributed by the near-bottom currents.

Vertical input from pelagic settling resulted in high content of coccoliths is registered during MIS 1 that is common for contourite muds and interglacial intervals in the North Atlantic (e.g. Ruddiman and McIntyre 1976; Bankole *et al.* 2020). Deposition of high-carbonate pelagite and diatom ooze during MIS 3 and glacial-interglacial transition (beginning of MIS 1), respectively, is supposed to be connected with the SAF – main hydrological front in the North Atlantic. Such fronts are characterised by elevated sea-surface primary production and are known as ‘hot spots’ of marine life (Belkin *et al.* 2009). During the Late Quaternary, position of the SAF underwent drastic changes that affected northern heat transport and Atlantic Meridional Overturning Circulation (e.g. Bolton *et al.* 2018; Perner *et al.* 2018). Our data suggest a location of SAF over the study area during some episodes of the MIS 3 – high values of total foraminiferal counts coinciding with increased IRD content (Figure 8). These episodes may be connected with unstable climate conditions of the intermediate glacial MIS 3 associated with prominent millennial-scale Dansgaard-Oeschger events. According to modelling results, these events are connected with the ocean surface freshwater fluxes related to ice sheet processes (Zhang and Prange 2020). The shifts of SAF location in the area of the Reykjanes Ridge result from the freshwater advection (e.g. Perner *et al.* 2018) and, therefore, could be conditioned by freshwater inputs during MIS 3. However, this suggestion needs additional studies.

Local distribution of diatom ooze and its absence in the sediments from the same period in the neighbouring sediment cores from IODP site 1304 (Channell *et al.* 2006; Hodell *et al.* 2010; Fagel and Mattielli 2011) may be explained by the topography of the contourite drift complicated by sedimentary dunes (Figure 7c) or/and by patchiness of the diatom mats on the sea-surface. However, the presence of the diatom mats through the sediments at IODP site U1304 supports the periodical presence of the SAF over the area during the Quaternary (Channell *et al.* 2006).

Hemipelagic settling provides IRD and volcanic ash components delivered from distal sources. Tephra layers of Icelandic origin are widely dispersed across the North Atlantic (e.g. Rutledal *et al.* 2020). High content of the IRD in the North Atlantic sediments is an indicator of glacial sedimentation and the ice-rafted material in the CGFZ area could have originated from Laurentide, Greenlandic, Icelandic, and Scandinavian Ice Sheets depending on the sea-surface paleocirculation pattern (e.g. Ruddiman 1977).

High seismic activity in the area (Aderhold and Abercrombie 2016; Skolotnev *et al.* 2021a; Sokolov *et al.* 2024) produces widely distributed sediments through downslope gravity flows in the CGFZ area (Figure 13). Turbidites and mass flow deposits of varying thickness were found in core V53-C1 and extensively in other sediment cores from the study area (Faugères *et al.* 1983; Bashirova *et al.* 2017). The fine-grained sediment material, delivered by distal gravity flows, is mainly redistributed by near-bottom currents in the area of contourite drifts. If the gravity flows are proximate to the drifts or occur during periods of inactive bottom currents, turbidite beds may be included in the contourite drift. Such occurrences were recorded on sub-bottom profiling records in the inactive southern valley (Figure 6h) and in core V53-C1 in the northern active valley (Figure 8).

### **Late Quaternary evolutionary stages**

*Depositional evolution during the Late Pleistocene to Holocene.* The two main depositional modes were recorded in the studied cores. According to the constructed age model, the current-controlled sedimentation corresponds with the interglacial (Holocene) period. In contrast, during cold and intermediate intervals of the last glaciation (MIS 2 and MIS 3) a dominance of hemipelagic deposition with intercalation of turbiditic and pelagic processes was registered (Figure 8, Figure 9, and Figure 11). Based on the sedimentary model (Figure 13), the contouritic sedimentation on the CGFZ valleys is mainly controlled by the flow of ISOW and possibly partially DSOW, which are the main components of the NADW (Worthington 1976). Late Quaternary variability in the formation of the NADW is believed to be closely linked with global climate changes and its circulation pattern is characterized by the glacial and interglacial end members (e.g., Broecker and Denton 1989; Sarnthein *et al.* 1994; Lisiecki *et al.* 2008). During the interglacial state (including the Holocene) the NADW is formed in the Nordic Seas and the flows of ISOW and DSOW are intensive. This circulation state agrees with our data on the current-controlled sedimentation in the valleys of the CGFZ (Figure 14a).

During glacial intervals, the convection in the Nordic Seas was greatly reduced and shallow water convection developed to the south of Iceland producing Glacial North Atlantic Intermediate Water (GNAIW) and allowing largely intrusion of the Glacial Antarctic Bottom Water (GAABW) to the North Atlantic (e.g., Sarnthein *et al.* 1994). The boundary between GNAIW and GAABW was at approximately 2000-2500 m depth (Sarnthein *et al.* 1994; Thornalley *et al.* 2010) resulting in domination of the GAABW over the CGFZ area (Figure 14b). Although our data do not provide

information about changes in deep water type over the study area, it clearly shows the decreasing of bottom current intensity at least in the northern valley and over the eastern flank of the Reykjanes during glacial interval. The absence of the current control on the deposition during MIS 3-2 in the studied sediment cores confirms the significant drop in the intensity of the NADW current (McCave *et al.* 1995b, a; McCave and Hall 2006; Elmore *et al.* 2015; Sivkov *et al.* 2015; McCave and Andrews 2019) and sluggish current of the GAABW in the North Atlantic during glacials (Manighetti and McCave 1995; Thornalley *et al.* 2010). Although a third end-member of deep water circulation was proposed for the Heinrich events with the absence of the GNAIW formation (e.g., Sarnthein *et al.* 1994; Rahmstorf 2002), our data do not allow us to distinguish between this short mode and glacial mode because of poor dating of the glacial sediments in the cores.

*Direction of the bottom current flow through time.* The direction of the bottom flow can be determined by mineralogical data providing information on particle province. Amphibole may serve as an indicator of a North American shield source in the North Atlantic during the Late Pleistocene–Holocene period (Fagel and Mattielli 2011). According to our mineralogical data, amphibole is present in core V53-C2 to at least 290 cm, which corresponds to ~11–10 cal ka BP (Figure 10c). In the southern core V53-C1, the presence of amphibole is recorded from the bottom of the core to a depth of 160 cm, which roughly corresponds with the Middle Holocene (Figure 10c). This shows the existence of the eastward bottom current flow during the Late Pleistocene–Middle Holocene in the valleys of the CGFZ and corresponds with sluggish westward ISOW flow and its subsequent gradual recovery during the cold MIS 2 and Early Holocene, respectively (Sarnthein *et al.* 1994; Kissel *et al.* 2009; Fagel and Mattielli 2011). Our data match well with the results of Fagel and Mattielli (2011) (Figure 2 and Figure 10c), who reported a deep-water connection between the Labrador Sea and the Iceland Basin through the CGFZ up to ~6 ka BP. The extended presence of amphibole in the sediments from the southern core (up to the Middle Holocene in V53-C1) compared with the northern core (up to the Early Holocene in V53-C2) (Figure 10c), indicates that eastern-sourced deep waters occurred for longer in the valleys of the CGFZ than further to the north in the Iceland Basin. This finding corresponds with a shallower position of the ISOW current during the Early Holocene than at present (Thornalley *et al.* 2013), which may promote the filling of the CGFZ valleys by eastward flowing LDW or DSOW. During the Late Pleistocene, only GAABW could have been responsible for the carrying of amphibole through CGFZ as it filled the transform valleys (Figure 14).

## Conclusions

In this work, we used seismo-acoustic profiling and lithological data to determine the sedimentary processes in the valleys of the CGFZ and the adjacent eastern flank of the Reykjanes Ridge. The channel-related mounded and sheeted drifts were recorded in the northern and southern inactive valleys. The ITD ridges and median ridges govern the position of the contourite channels and moats in this system. Plastered drift was found along the southern wall of the northern active valley and its position is proposed to be linked with tectonic processes in the active transform. Confined drift was detected in the isolated depression on the eastern flank of Reykjanes Ridge. Vast-spread sediment dunes and waves indicate bottom current activity over the drifts.

Considering the depths of the contourite drifts and modern circulation pattern, we have inferred that the ISOW current is responsible for the formation of the drifts in the isolated depression on the eastern flank of the Reykjanes Ridge, in the northern valley, and in the eastern part of the southern



inactive valley. The contourite sedimentation in the western part of the southern inactive valley is governed mainly under the influence of the deeper, eastward-flowing LDW or DSOW.

Based on the studies of two sediment cores, we have found that contourite drifts consist of alternated muddy and silty contourites and pelagic/hemipelagic sediments rather than pure contourites. We have inferred that this intercalation is caused by changes in the circulation pattern in the North Atlantic Ocean linked to global climate changes. The alternation of the contouritic and hemipelagic/pelagic deposition is proposed to be reflected in the acoustically layered structure of the drifts.

The contourite deposition with high accumulation rates (averaging 19–24 cm/kyr) corresponds to the recent interglacial interval and very likely to the Late Quaternary interglacials. The gradual increase in the westward-flowing ISOW current from the Late Pleistocene to the Middle Holocene was revealed based on the mineralogical data showing consistent disappearance of amphibole from the sediments. The current-controlled deposition occurred simultaneously with a high input of biogenic material resulting from pelagic settling.

Pelagic/hemipelagic sedimentation prevailed during cold intervals (MIS 3-2) and the last glacial/interglacial transition and corresponds with high IRD content in the sediments. The position of highly productive SAF over the study area induced the formation of diatom ooze beds at the beginning of MIS 1 and high-carbonate pelagites during some intervals of MIS 3. Depositional units related to short-term events were also found in the studied sediment cores. A turbidite bed reflects the local gravitational processes common in the study area and tephra layers (North Atlantic Ash Zone 1) were formed due to volcanic eruptions in Iceland.

This study sheds light on sedimentation processes in the fracture zone, which serves as a deep-water passage for the northern-sourced ISOW. The hydrology of deep waters of northern origin and their climatic variability in the North Atlantic are well studied. However, the degree of influence of deep waters of southern origin remains poorly understood and requires further research. In addition, we focused on the Late Quaternary interval of sedimentation history, but the pre-Quaternary period remains poorly understood. This raises questions about the relationship between tectonic evolution and sedimentation in the fracture zone, which are addressed to future studies.

### **Funding**

Study of sediment cores and palaeoclimate reconstructions were financed by RSF, grant No. 22-17-00170, <https://rscf.ru/project/22-17-00170/>. The interpretation of the seismo-acoustic profiler data was done with the support of the state assignment of IO RAS (Theme No. FMWE-2021-0012).

## **Acknowledgements**

We wish to thank the two anonymous reviewers for their constructive and detailed comments that helped to significantly improve this paper. We would like to express deep gratitude to Prof. F. Javier Hernández-Molina for his very constructive recommendations and valuable comments and also for the smooth editorial handling. We greatly appreciate the support of Dr Vadim Sivkov and Dr Dmitriy Dorokhov and the fruitful discussion about the manuscript. We are very grateful to Tatiana Glazkova for her thorough English editing of the early versions of the manuscript.

ACCEPTED MANUSCRIPT

## References

- Aderhold, K. and Abercrombie, R.E. 2016. The 2015 Mw 7.1 earthquake on the Charlie-Gibbs transform fault: Repeating earthquakes and multimodal slip on a slow oceanic transform. *Geophysical Research Letters*, **43**, 6119–6128, <https://doi.org/10.1002/2016GL068802>.
- Bankole, S., Buckman, J. and Stow, D. 2020. Unusual components within a fine-grained contourite deposit: Significance for interpretation of provenance and the contourite budget. *Minerals*, **10**, <https://doi.org/10.3390/min10060488>.
- Bashirova, L.D., Dorokhova, E.V., Sivkov, V.V., Andersen, N., Kuleshova, L.A. and Matul, A.G. 2017. Paleocurrents in the Charlie-Gibbs Fracture Zone during the Late Quaternary. *Oceanology*, **57**, <https://doi.org/10.1134/S0001437017020035>.
- Belkin, I.M., Cornillon, P.C. and Sherman, K. 2009. Fronts in Large Marine Ecosystems. *Progress in Oceanography*, **81**, 223–236, <https://doi.org/10.1016/j.pocean.2009.04.015>.
- Berner, R.A. 1982. Burial of organic carbon and pyrite sulfur in the modern ocean. *American Journal of Science*, **282**, 451–473.
- Bianchi, G.G. and McCave, I.N. 2000. Hydrography and sedimentation under the deep western boundary current on Björn and Gardar Drifts, Iceland Basin. *Marine Geology*, **165**, 137–169, [https://doi.org/10.1016/S0025-3227\(99\)00139-5](https://doi.org/10.1016/S0025-3227(99)00139-5).
- Bodén, P. and Backman, J. 1996. A laminated sediment sequence from the northern North Atlantic Ocean and its climatic record. *Geology*, **24**, 507–510, [https://doi.org/10.1130/0091-7613\(1996\)024<0507:ALSSFT>2.3.CO;2](https://doi.org/10.1130/0091-7613(1996)024<0507:ALSSFT>2.3.CO;2).
- Bolton, C.T., Bailey, I., et al. 2018. North Atlantic Midlatitude Surface-Circulation Changes Through the Plio-Pleistocene Intensification of Northern Hemisphere Glaciation. *Paleoceanography and Paleoclimatology*, **33**, 1186–1205, <https://doi.org/10.1029/2018PA003412>.
- Bond, G., Heinrich, H., et al. 1992. Evidence for massive discharges of icebergs into the North Atlantic ocean during the last glacial period. *Nature*, **360**, 245–249, <https://doi.org/10.1038/360245a0>.
- Borisov, D.G., Frey, D.I., Ivanova, E. V., Dmitrevskiy, N.N., Levchenko, O. V., Fomin, V. V. and Ligi, M. 2023. Unveiling the contourite depositional system in the Vema Fracture Zone (Central Atlantic). *Scientific Reports*, **13**, 1–12, <https://doi.org/10.1038/s41598-023-40401-4>.
- Bower, A. and Furey, H. 2017. Iceland-Scotland Overflow Water transport variability through the Charlie-Gibbs Fracture Zone and the impact of the North Atlantic Current. *Journal of Geophysical Research: Oceans*, **122**, 6989–7012, <https://doi.org/10.1002/2017JC012698>.
- Boyle, J.F., Chiverrell, R.C. and Schillereff, D. 2015. Approaches to Water Content Correction and Calibration for  $\mu$ XRF Core Scanning: Comparing X-ray Scattering with Simple Regression of Elemental Concentrations. In: Croudace, I. and Rothwell, R. (eds) *Micro-XRF Studies of Sediment Cores. Developments in Paleoenvironmental Research, Vol 17*. 373–390., [https://doi.org/10.1007/978-94-017-9849-5\\_14](https://doi.org/10.1007/978-94-017-9849-5_14).
- Brackenridge, R.E., Stow, D.A.V., et al. 2018. Textural characteristics and facies of sand-rich contourite depositional systems. *Sedimentology*, <https://doi.org/10.1111/sed.12463>.
- Broecker, W.S. and Denton, G.H. 1989. The role of ocean-atmosphere reorganizations in glacial cycles. *Geochimica et Cosmochimica Acta*, **53**, 2465–2501, [https://doi.org/10.1016/0016-7037\(89\)90123-3](https://doi.org/10.1016/0016-7037(89)90123-3).

- Broecker, W.S., Peteet, D.M. and Rind, D. 1985. Does the ocean-atmosphere system have more than one stable mode of operation? *Nature*, **315**, 21–26, <https://doi.org/10.1038/315021a0>.
- Channell, J.E.T., Kanamatsu, T., Sato, T., Stein, T., Alvarez Zarikian, C.A., Malone, M.J. and Scientists, and E. 303/306. 2006. Site U1304. *In: Proceedings of the IODP, 303/306*. 1–82., <https://doi.org/10.2204/iodp.proc.303306.104.2006>.
- Chernysheva, E.A. and Kharin, G.S. 2009. Magmatic rocks in the Charlie-Gibbs Fracture Zone, North Atlantic Ocean. *Petrology*, **17**, 476–487, <https://doi.org/10.1134/S0869591109050038>.
- Cremer, M., Faugères, J.C., Grousset, F. and Gonthier, E. 1993. Late Quaternary sediment flux on sedimentary drifts in the Northeast Atlantic. *Sedimentary Geology*, **82**, 89–101, [https://doi.org/10.1016/0037-0738\(93\)90115-L](https://doi.org/10.1016/0037-0738(93)90115-L).
- Croudace, I.W. and Rothwell, R.G. 2015. *Micro-XRF Studies of Sediment Cores*, Developmen. Croudace, I. W. and Rothwell, R. G. (eds), <https://doi.org/10.1007/978-94-017-9849-5>.
- Damuth, J.E. 1980. Use of high-frequency (3.5–12 kHz) echograms in the study of near-bottom sedimentation processes in the deep-sea: A review. *Marine Geology*, **38**, 51–75, [https://doi.org/10.1016/0025-3227\(80\)90051-1](https://doi.org/10.1016/0025-3227(80)90051-1).
- Damuth, J.E. and Hayes, D.E. 1977. Echo character of the East Brazilian continental margin and its relationship to sedimentary processes. *Marine Geology*, **24**, 73–95, [https://doi.org/10.1016/0025-3227\(77\)90002-0](https://doi.org/10.1016/0025-3227(77)90002-0).
- Dang, Z., Zhang, N., Li, Z.X., Huang, C., Spencer, C.J. and Liu, Y. 2020. Weak orogenic lithosphere guides the pattern of plume-triggered supercontinent break-up. *Communications Earth and Environment*, **1**, 1–12, <https://doi.org/10.1038/s43247-020-00052-z>.
- Daniault, N., Mercier, H., et al. 2016. The northern North Atlantic Ocean mean circulation in the early 21st century. *Progress in Oceanography*, **146**, 142–158, <https://doi.org/10.1016/j.pocean.2016.06.007>.
- Davies, T. and Laughton, A. 1972. Sedimentary processes in the north Atlantic. *Initial reports of the deep sea drilling project*, 905–934.
- de Castro, S., Hernández-Molina, F.J., et al. 2021. Contourite characterization and its discrimination from other deep-water deposits in the Gulf of Cadiz contourite depositional system. *Sedimentology*, **68**, 987–1027, <https://doi.org/https://doi.org/10.1111/sed.12813>.
- Dobrolyubov, S.A., Lappo, S.S., Morozov, E.G. and Sokov, A. V. 2003. Water transport through the Charlie-Gibbs Fracture Zone. *Doklady Earth Sciences*, **391**, 903–905.
- Elmore, A.C., Wright, J.D. and Chalk, T.B. 2015. Precession-driven changes in Iceland-Scotland Overflow Water penetration and bottom water circulation on Gardar Drift since ~200ka. *Palaeogeography, Palaeoclimatology, Palaeoecology*, **440**, 551–563, <https://doi.org/10.1016/j.palaeo.2015.09.042>.
- Esentia, I., Stow, D. and Smillie, Z. 2018. Contourite Drifts and Associated Bedforms. 301–331., [https://doi.org/10.1007/978-3-319-57852-1\\_16](https://doi.org/10.1007/978-3-319-57852-1_16).
- Fagel, N. and Mattielli, N. 2011. Holocene evolution of deep circulation in the northern North Atlantic traced by Sm, Nd and Pb isotopes and bulk sediment mineralogy. *Paleoceanography*, **26**, 1–15, <https://doi.org/10.1029/2011PA002168>.

- Faugères, J.C. and Mulder, T. 2011. Contour currents and contourite drifts. *Developments in Sedimentology*, **63**, 149–214, <https://doi.org/10.1016/B978-0-444-53000-4.00003-2>.
- Faugères, J.C., Gonthier, E. and Poutiers, J. 1983. Facies and sediment dynamics in Charlie-Gibbs fracture zone during the Late Quaternary. *Marine Geology*, **52**, 101–119, [https://doi.org/10.1016/0025-3227\(83\)90023-3](https://doi.org/10.1016/0025-3227(83)90023-3).
- Faugères, J.C., Stow, D.A. V, Imbert, P. and Viana, A. 1999. Seismic features diagnostic of contourite drifts. *Marine Geology*, **162**, 1–36.
- Fleming, H.S., Cherkis, N.Z. and Heirtzler, J.R. 1970. The Gibbs Fracture Zone: A double fracture zone at 52°30'N in the Atlantic Ocean. *Marine Geophysical Researches*, **1**, 37–45, <https://doi.org/10.1007/BF00310008>.
- García, M., Hernández-Molina, F.J., et al. 2009. Contourite erosive features caused by the Mediterranean Outflow Water in the Gulf of Cadiz: Quaternary tectonic and oceanographic implications. *Marine Geology*, **257**, 24–40, <https://doi.org/10.1016/j.margeo.2008.10.009>.
- Glazkova, T., Hernández-Molina, F.J., et al. 2022. Sedimentary processes in the Discovery Gap (Central–NE Atlantic): An example of a deep marine gateway. *Deep Sea Research Part I: Oceanographic Research Papers*, **180**, 103681, <https://doi.org/10.1016/j.dsr.2021.103681>.
- Gonçalves Neto, A., Palter, J.B., Bower, A., Furey, H. and Xu, X. 2020. Labrador Sea Water Transport Across the Charlie-Gibbs Fracture Zone. *Journal of Geophysical Research: Oceans*, **125**, <https://doi.org/10.1029/2020JC016068>.
- Heaton, T.J., Köhler, P., et al. 2020. Marine20 - The Marine Radiocarbon Age Calibration Curve (0–55,000 cal BP). *Radiocarbon*, **62**, 779–820, <https://doi.org/10.1017/RDC.2020.68>.
- Helmke, J.P. and Bauch, H.A. 2001. Glacial-interglacial relationship between carbonate components and sediment reflectance in the North Atlantic. *Geo-Marine Letters*, **21**, 16–22, <https://doi.org/10.1007/s003670100067>.
- Hensen, C., Duarte, J.C., et al. 2019. Marine transform faults and fracture zones: A joint perspective integrating seismicity, fluid flow and life. *Frontiers in Earth Science*, **7**, 1–29, <https://doi.org/10.3389/feart.2019.00039>.
- Hernández-Molina, F.J., Maldonado, A. and Stow, D.A.V. 2008. Chapter 18 Abyssal Plain Contourites. *Developments in Sedimentology*, **60**, [https://doi.org/10.1016/S0070-4571\(08\)10018-8](https://doi.org/10.1016/S0070-4571(08)10018-8).
- Hodell, D.A., Evans, H.F., Channell, J.E.T. and Curtis, J.H. 2010. Phase relationships of North Atlantic ice-rafted debris and surface-deep climate proxies during the last glacial period. *Quaternary Science Reviews*, **29**, 3875–3886, <https://doi.org/10.1016/j.quascirev.2010.09.006>.
- Hunt, J.E., Croudace, I.W. and MacLachlan, S.E. 2015. Use of Calibrated ITRAX XRF Data in Determining Turbidite Geochemistry and Provenance in Agadir Basin, Northwest African Passive Margin. In: *Micro-XRF Studies of Sediment Cores*. 127–146., [https://doi.org/10.1007/978-94-017-9849-5\\_4](https://doi.org/10.1007/978-94-017-9849-5_4).
- Johnson, L.G. 1967. North atlantic fracture zones near 53°. *Earth and Planetary Science Letters*, **2**, 445–448, [https://doi.org/10.1016/0012-821X\(67\)90187-2](https://doi.org/10.1016/0012-821X(67)90187-2).
- Kemp, A.E.S., Baldauf, J.G. and Pearce, R.B. 1996. Origins and palaeoceanographic significance of laminated daitom ooze from the Eastern Equatorial Pacific Ocean. *Geological Society Special Publication*, **116**, 243–252, <https://doi.org/10.1144/GSL.SP.1996.116.01.19>.

- Keogh, P., Command, R.J., Edinger, E., Georgiopoulou, A. and Robert, K. 2022. Benthic megafaunal biodiversity of the Charlie-Gibbs fracture zone: spatial variation, potential drivers, and conservation status. *Marine Biodiversity*, **52**, <https://doi.org/10.1007/s12526-022-01285-1>.
- Kissel, C., Laj, C., Mulder, T., Wandres, C. and Cremer, M. 2009. The magnetic fraction: A tracer of deep water circulation in the North Atlantic. *Earth and Planetary Science Letters*, **288**, 444–454, <https://doi.org/10.1016/j.epsl.2009.10.005>.
- Kissel, C., Van Toer, A., Laj, C., Cortijo, E. and Michel, E. 2013. Variations in the strength of the North Atlantic bottom water during Holocene. *Earth and Planetary Science Letters*, **369–370**, 248–259, <https://doi.org/10.1016/j.epsl.2013.03.042>.
- Krauss, W. 1986. The North Atlantic Current. *Journal of Geophysical Research: Oceans*, **91**, 5061–5074, <https://doi.org/10.1029/JC091iC04p05061>.
- Kuhn, G. and Weber, M.E. 1993. Acoustical characterization of sediments by Parasound and 3.5 kHz systems: Related sedimentary processes on the southeastern Weddell Sea continental slope, Antarctica. *Marine Geology*, **113**, 201–217, [https://doi.org/10.1016/0025-3227\(93\)90018-Q](https://doi.org/10.1016/0025-3227(93)90018-Q).
- Le Pichon, X., Eittrheim, S. and Ewing, J. 1971a. A sedimentary channel along Gibbs Fracture Zone. *Journal of Geophysical Research*, **76**, 2891–2896, <https://doi.org/10.1029/JC076i012p02891>.
- Le Pichon, X., Eittrheim, S. and Ewing, J. 1971b. Reply [to “Discussion of paper by X. Le Pichon, S. Eittrheim, and J. Ewing, ‘A sedimentary channel along Gibbs Fracture Zone’”]. *Journal of Geophysical Research*, **76**, 6609–6612, <https://doi.org/10.1029/jc076i027p06609>.
- Ligi, M., Bonatti, E., Gasperini, L. and Poliakov, A.N.B. 2002. Oceanic broad multifault transform plate boundaries. *Geology*, **30**, 11–14, [https://doi.org/10.1130/0091-7613\(2002\)030<0011:OBMTPB>2.0.CO;2](https://doi.org/10.1130/0091-7613(2002)030<0011:OBMTPB>2.0.CO;2).
- Lilwall, R.C. and Kirk, R.E. 1985. Ocean-bottom seismograph observations on the Charlie—Gibbs fracture zone. *Geophysical Journal of the Royal Astronomical Society*, **80**, 195–208, <https://doi.org/10.1111/j.1365-246X.1985.tb05085.x>.
- Lisiecki, L.E., Raymo, M.E. and Curry, W.B. 2008. Atlantic overturning responses to Late Pleistocene climate forcings. *Nature*, **456**, 85–88, <https://doi.org/10.1038/nature07425>.
- Lonsdale, P. and Shor, A. 1979. The oblique intersection of the Mid-Atlantic Ridge with Charlie-Gibbs transform fault. *Tectonophysics*, **54**, 195–209, [https://doi.org/10.1016/0040-1951\(79\)90368-8](https://doi.org/10.1016/0040-1951(79)90368-8).
- Manighetti, B. and McCave, I.N. 1995. Late Glacial and Holocene palaeocurrents around Rockall Bank, NE Atlantic Ocean. *Paleoceanography*, **10**, 611–626, <https://doi.org/10.1029/94PA03059>.
- McCartney, M.S. 1992. Recirculating components to the deep boundary current of the northern North Atlantic. *Progress in Oceanography*, **29**, 283–383, [https://doi.org/10.1016/0079-6611\(92\)90006-L](https://doi.org/10.1016/0079-6611(92)90006-L).
- McCave, I.N. and Andrews, J.T. 2019. Distinguishing current effects in sediments delivered to the ocean by ice. II. Glacial to Holocene changes in high latitude North Atlantic upper ocean flows. *Quaternary Science Reviews*, **223**, 105902, <https://doi.org/10.1016/j.quascirev.2019.105902>.
- McCave, I.N. and Hall, I.R. 2006. Size sorting in marine muds: Processes, pitfalls, and prospects for paleoflow-speed proxies. *Geochemistry, Geophysics, Geosystems*, **7**, 1–37, <https://doi.org/10.1029/2006GC001284>.

- McCave, I.N., Manighetti, B. and Beveridge, N.A.S. 1995a. Circulation in the glacial North Atlantic inferred from grain-size measurements. *Nature*, **374**, 149–152, <https://doi.org/10.1038/374149a0>.
- McCave, I.N., Manighetti, B. and Robinson, S.G. 1995b. Sortable Silt and Fine Sediment Size Composition Slicing - Parameters for Paleocurrent Speed and Paleoceanography. *Paleoceanography*, **10**, 593–610, <https://doi.org/10.1029/94PA03039>.
- McIntyre, A., Ruddiman, W.F. and Jantzen, R. 1972. Southward penetrations of the North Atlantic Polar Front: faunal and floral evidence of large-gale surface water mass movements over the last 225,000 years. *Deep Sea Research and Oceanographic Abstracts*, **19**, 61–77, [https://doi.org/https://doi.org/10.1016/0011-7471\(72\)90073-3](https://doi.org/https://doi.org/10.1016/0011-7471(72)90073-3).
- Mitchell, N.C. 2018. Mid-ocean Ridges. In: Micallef, A., Krastel, S. and Savini, A. (eds) *Submarine Geomorphology*. Springer Geology, 349–365., [https://doi.org/10.1007/978-3-319-57852-1\\_18](https://doi.org/10.1007/978-3-319-57852-1_18).
- Moore, D.G. 1969. Reflection profiling studies of the California Continental Borderland;: Structure and Quaternary turbidite basins. *Geological Society of America. Special paper*, **107**, 0–142.
- Morozov, E.G., Demidov, A.N., Tarakanov, R.Y. and Zenk, W. 2010. *Abyssal Channels in the Atlantic Ocean*, <https://doi.org/10.1007/978-90-481-9358-5>.
- Müller, R.D., Sdrolias, M., Gaina, C. and Roest, W.R. 2008. Age, spreading rates, and spreading asymmetry of the world's ocean crust. *Geochemistry, Geophysics, Geosystems*, **9**, <https://doi.org/10.1029/2007GC001743>.
- Olivet, J.-L., Le Pichon, X., Monti, S. and Sichler, B. 1974. Charlie-Gibbs Fracture Zone. *Journal of Geophysical Research*, **79**, 2059–2072, <https://doi.org/10.1029/JB079i014p02059>.
- Perner, K., Moros, M., Jansen, E., Kuijpers, A., Troelstra, S.R. and Prins, M.A.A.R.T.I.N.A. 2018. Subarctic Front migration at the Reykjanes Ridge during the mid- to late Holocene: evidence from planktic foraminifera. *Boreas*, **47**, 175–188, <https://doi.org/10.1111/bor.12263>.
- Petit, T. 2018. Characterization of the circulation around, above and across (through fracture zones) the Reykjanes Ridge. 1–201.
- Priede, I.G., Billett, D.S.M., et al. 2013. The ecosystem of the Mid-Atlantic Ridge at the sub-polar front and Charlie-Gibbs Fracture Zone; ECO-MAR project strategy and description of the sampling programme 2007-2010. *Deep-Sea Research Part II: Topical Studies in Oceanography*, **98**, 220–230, <https://doi.org/10.1016/j.dsr2.2013.06.012>.
- Pushcharovskiy, Y.M., Peive, A.A., Raznicin, Y.N. and Bazilevskaya, E.S. 1995. Fault zones in the Central Atlantic. *Trudy GIN*, **495**, 160.
- Racapé, V., Thierry, V., Mercier, H. and Cabanes, C. 2019. ISOW Spreading and Mixing as Revealed by Deep-Argo Floats Launched in the Charlie-Gibbs Fracture Zone. *Journal of Geophysical Research: Oceans*, **124**, 6787–6808, <https://doi.org/10.1029/2019JC015040>.
- Rahmstorf, S. 2002. Ocean circulation and climate during the past 120,000 years. *Nature*, **419**, 207–214, <https://doi.org/10.1038/nature01090>.
- Rebesco, M. and Stow, D. 2001. Seismic expression of contourites and related deposits: A preface. *Marine Geophysical Research*, **22**, 303–308, <https://doi.org/10.1023/A:1016316913639>.
- Rebesco, M., Hernández-Molina, F.J., Van Rooij, D. and Wåhlin, A. 2014. Contourites and associated

- sediments controlled by deep-water circulation processes: State-of-the-art and future considerations. *Marine Geology*, **352**, 111–154, <https://doi.org/10.1016/j.margeo.2014.03.011>.
- Richardson, M.D. and Briggs, K.B. 1993. On the Use of Acoustic Impedance Values to Determine Sediment Properties Effects of Hypoxia on Sediment Properties View project Completed View project.
- Ruddiman, W.F. 1972. Sediment Redistribution on the Reykjanes Ridge: Seismic Evidence. *Geological Society of America Bulletin*, **83**, 2039–2062, <https://doi.org/10.1130/0016-7606>.
- Ruddiman, W.F. 1977. Late Quaternary deposition of ice-rafted sand in the subpolar North Atlantic (lat 40° to 65°N). *Bulletin of the Geological Society of America*, **88**, 1813–1827, [https://doi.org/10.1130/0016-7606\(1977\)88<1813:LQDOIS>2.0.CO;2](https://doi.org/10.1130/0016-7606(1977)88<1813:LQDOIS>2.0.CO;2).
- Ruddiman, W.F. and McIntyre, A. 1976. Northeast Atlantic paleoclimatic changes over the past 600,000 years. *Memoir of the Geological Society of America*, **145**, 111–146, <https://doi.org/10.1130/MEM145-p111>.
- Rutledal, S., Berben, S.M.P., Dokken, T.M., van der Bilt, W.G.M., Cederstrøm, J.M. and Jansen, E. 2020. Tephra horizons identified in the western North Atlantic and Nordic Seas during the Last Glacial Period: Extending the marine tephra framework. *Quaternary Science Reviews*, **240**, 106247, <https://doi.org/10.1016/j.quascirev.2020.106247>.
- Sarnthein, M., Winn, K., Jung, S.J.A., Duplessy, J.-C., Labeyrie, L., Erlenkeuser, H. and Ganssen, G. 1994. Changes in East Atlantic Deepwater Circulation over the last 30,000 years: Eight time slice reconstructions. *Paleoceanography*, **9**, 209–267, <https://doi.org/10.1029/93PA03301>.
- Saunders, P.M. 1994. The flux of overflow water through the Charlie-Gibbs Fracture Zone. *Journal of Geophysical Research*, **99**, <https://doi.org/10.1029/94jc00527>.
- Schaeffer, A.J. and Lebedev, S. 2013. Global shear speed structure of the upper mantle and transition zone. *Geophysical Journal International*, **194**, 417–449, <https://doi.org/10.1093/gji/ggt095>.
- Schott, F., Stramma, L. and Fischer, J. 1999. Interaction of the North Atlantic Current with the Deep Charlie Gibbs Fracture Zone Throughflow. *Geophysical Research Letters*, **26**, 369–372, <https://doi.org/10.1029/1998GL900223>.
- Searle, R. 1981. The active part of Charlie-Gibbs Fracture Zone: a study of sonar and other geophysical techniques. **86**, 243–262.
- Searle, R.C. 1979. Side-scan sonar studies of North Atlantic fracture zones. *Journal of the Geological Society*, **136**, 283–291, <https://doi.org/10.1144/gsjgs.136.3.0283>.
- Shepard, F.P. 1954. Nomenclature Based on Sand-silt-clay Ratios. *SEPM Journal of Sedimentary Research*, **Vol. 24**, 256, <https://doi.org/10.1306/D4269774-2B26-11D7-8648000102C1865D>.
- Shor, A., Lonsdale, P., Hollister, C.D. and Spencer, D. 1980. Charlie-Gibbs fracture zone: bottom-water transport and its geological effects. *Deep Sea Research Part A. Oceanographic Research Papers*, **27**, 325–345, [https://doi.org/10.1016/0198-0149\(80\)90030-8](https://doi.org/10.1016/0198-0149(80)90030-8).
- Sivkov, V.V., Dorokhova, E.V. and Bashirova, L.D. 2015. Contour currents of the North Atlantic during the last glacial cycle. *Oceanology*, **55**, <https://doi.org/10.1134/S0001437015060181>.
- Skolotnev, S.G., Sanfilippo, A., et al. 2020. New Data on the Structure of the Megatransform System



- of the Doldrums (Central Atlantic). *Doklady Earth Sciences*, **491**, 131–134, <https://doi.org/10.1134/S1028334X20030186>.
- Skolotnev, S.G., Sanfilippo, A., et al. 2021a. Geological and Geophysical Studies of the Charlie Gibbs Fracture Zone (North Atlantic). *Doklady Earth Sciences*, **497**, 191–194, <https://doi.org/10.1134/s1028334x21030107>.
- Skolotnev, S.G., Sanfilippo, A., et al. 2021b. Seafloor spreading and tectonics at the Charlie Gibbs transform system (52–53°N, Mid Atlantic Ridge): Preliminary results from R/V A. N. Strakhov expedition S50. *Ofioliti*, **46**, 83–101, <https://doi.org/10.4454/ofioliti.v46i1.539>.
- Skolotnev, S.G., Sanfilippo, A., et al. 2023. Crustal Accretion Along the Northern Mid Atlantic Ridge (52°–57°N): Preliminary Results From Expedition V53 of R/V Akademik Sergey Vavilov. *Ofioliti*, **48**, 13–30, <https://doi.org/10.4454/ofioliti.v48i1.559>.
- Smith, D. and Jabour, J. 2018. MPAs in ABNJ: Lessons from two high seas regimes. *ICES Journal of Marine Science*, **75**, 417–425, <https://doi.org/10.1093/icesjms/fsx189>.
- Sokolov, S.Y., Chamov, N.P., Khutorskoy, M.D. and Silantiev, S.A. 2020. Intensity indicators of geodynamic processes along the Atlantic-Arctic rift system. *Geodynamics & Tectonophysics*, **11**, 302–319, <https://doi.org/10.5800/GT-2020-11-2-0476>.
- Sokolov, S.Y., Dobrolyubova, K.O. and Turko, N.N. 2022. Relationships of Surface Geological and Geophysical Characteristics with the Deep Structure of the Mid-Atlantic Ridge According to Seismic Tomography Data. *Geotectonics*, **56**, 107–122, <https://doi.org/10.1134/S0016852122020066>.
- Sokolov, S.Y., Denisova, A.P. and Patina, I.S. 2024. Geodynamic Setting of the Passive Part of the Charlie Gibbs Twin Transform Fault (North Atlantic). *Doklady Earth Sciences*, <https://doi.org/10.1134/S1028334X24601561>.
- Stoker, M.S., Akhurst, M.C., Howe, J.A. and Stow, D.A. V. 1998. Sediment drifts and contourites on the continental margin off northwest Britain. **115**, 33–51.
- Storey, B.C. 1995. The role of mantle plumes in continental breakup: case histories from Gondwanaland. *Nature*, **377**, 301–308, <https://doi.org/10.1038/377301a0>.
- Stow, D. and Smillie, Z. 2020. Distinguishing between deep-water sediment facies: Turbidites, contourites and hemipelagites. *Geosciences (Switzerland)*, **10**, <https://doi.org/10.3390/geosciences10020068>.
- Stow, D.A.V. and Faugères, J.C. 2008. Contourite Facies and the Facies Model. *Developments in Sedimentology*, **60**, 223–256, [https://doi.org/10.1016/S0070-4571\(08\)10013-9](https://doi.org/10.1016/S0070-4571(08)10013-9).
- Stow, D.A.V., Faugères, J.C., et al. 2002. Faro-Albufeira drift complex, northern Gulf of Cadiz. *Geological Society Memoir*, **22**, 137–154, <https://doi.org/10.1144/GSL.MEM.2002.022.01.11>.
- Stow, D.A.V., Hernández-Molina, F.J., Llave, E., Sayago-Gil, M., Díaz-del Río, V. and Branson, A. 2009. Bedform-velocity matrix: The estimation of bottom current velocity from bedform observations. *Geology*, **37**, 327–330, <https://doi.org/10.1130/G25259A.1>.
- Stow, D.A. V. and Tabrez, A.R. 1998. Hemipelagites: processes, facies and model. *Geological Society, London, Special Publications*, **129**, 317–337, <https://doi.org/10.1144/GSL.SP.1998.129.01.19>.
- Stow, D.A. V and Piper, D.J.W. 1984. Deep-water fine-grained sediments; history, methodology and

- terminology. *Geological Society, London, Special Publications*, **15**, 3–14, <https://doi.org/10.1144/GSL.SP.1984.015.01.01>.
- Thornalley, D.J.R., Elderfield, H. and McCave, I.N. 2010. Intermediate and deep water paleoceanography of the northern North Atlantic over the past 21,000 years. *Paleoceanography*, **25**, 1–17, <https://doi.org/10.1029/2009PA001833>.
- Thornalley, D.J.R., McCave, I.N. and Elderfield, H. 2011. Tephra in deglacial ocean sediments south of Iceland: Stratigraphy, geochemistry and oceanic reservoir ages. *Journal of Quaternary Science*, **26**, 190–198, <https://doi.org/10.1002/jqs.1442>.
- Thornalley, D.J.R., Blaschek, M., et al. 2013. Long-term variations in Iceland–Scotland overflow strength during the Holocene. *Climate of the Past*, **9**, 2073–2084, <https://doi.org/10.5194/cp-9-2073-2013>.
- Trentesaux, A., Recourt, P., Bout-Roumazielles, V. and Tribovillard, N. 2001. Carbonate Grain-Size Distribution in Hemipelagic Sediments from a Laser Particle Sizer. *Journal of Sedimentary Research*, **71**, 858–862, <https://doi.org/10.1306/2DC4096E-0E47-11D7-8643000102C1865D>.
- Van Andel, T.H. and Komar, P.D. 1969. Ponded Sediments of the Mid-Atlantic Ridge between 22° and 23° North Latitude. *Geological Society of America Bulletin*, **80**, 1163–1190, [https://doi.org/10.1130/0016-7606\(1969\)80\[1163:PSOTMR\]2.0.CO;2](https://doi.org/10.1130/0016-7606(1969)80[1163:PSOTMR]2.0.CO;2).
- Vogt, P.R. and Johnson, G.L. 1975. Transform faults and longitudinal flow below the Midoceanic Ridge. *Journal of Geophysical Research*, **80**, 1399–1428, <https://doi.org/10.1029/jb080i011p01399>.
- Walker, M., Johnsen, S., et al. 2009. Formal definition and dating of the GSSP (Global Stratotype Section and Point) for the base of the Holocene using the Greenland NGRIP ice core, and selected auxiliary records. *Journal of Quaternary Science*, **24**, 3–17, <https://doi.org/10.1002/jqs.1227>.
- Wentworth, C.K. 1922. A scale of grade and class terms for clastic sediments. *Journal of Geology*, **30**, 377–392.
- Worthington, L.V. 1976. *On the North Atlantic Circulation*.
- Worthington, L.V. and Volkmann, G.H. 1965. The volume transport of the Norwegian Sea overflow water in the North Atlantic. *Deep Sea Research and Oceanographic Abstracts*, **12**, 667–668, [https://doi.org/10.1016/0011-7471\(65\)91865-6](https://doi.org/10.1016/0011-7471(65)91865-6).
- Worthington, L. V. and Wright, W.R. 1971. Discussion [of paper by X. Le Pichon, S. Eittrheim, and J. Ewing, “A sedimentary channel along Gibbs Fracture Zone”]. *Journal of Geophysical Research*, **76**, 6606–6608, <https://doi.org/10.1029/JC076i027p06606>.
- Xu, X., Bower, A., Furey, H. and Chassignet, E.P. 2018. Variability of the Iceland-Scotland Overflow Water Transport Through the Charlie-Gibbs Fracture Zone: Results From an Eddy Simulation and Observations. *Journal of Geophysical Research: Oceans*, **123**, 5808–5823, <https://doi.org/10.1029/2018JC013895>.
- Yu, X., Stow, D., et al. 2020. Contourite porosity, grain size and reservoir characteristics. *Marine and Petroleum Geology*, **117**, 104392, <https://doi.org/10.1016/j.marpetgeo.2020.104392>.
- Zhang, X. and Prange, M. 2020. Stability of the Atlantic overturning circulation under intermediate (MIS3) and full glacial (LGM) conditions and its relationship with Dansgaard-Oeschger climate

variability. *Quaternary Science Reviews*, **242**, 106443,  
<https://doi.org/10.1016/j.quascirev.2020.106443>.

Zou, S., Bower, A., Furey, H., Susan Lozier, M. and Xu, X. 2020. Redrawing the Iceland–Scotland Overflow Water pathways in the North Atlantic. *Nature Communications*, **11**,  
<https://doi.org/10.1038/s41467-020-15513-4>.

ACCEPTED MANUSCRIPT

## Figure Captions

Figure 1. Generalised scheme of the circulation pattern in the subpolar North Atlantic Ocean based on Daniault *et al.* (2016) and the location of the CGFZ. The position of Subarctic Front (SAF) is according to Perner *et al.* (2018). Study area is indicated by the white box. The green-coloured area denotes the Gardar Drift. Topography: MAR - Mid-Atlantic Ridge, CGFZ - Charlie-Gibbs Fracture Zone, and WEB - Western European Basin. Circulation: NAC - North Atlantic Current, LSW - Labrador Sea Water, ISOW - Iceland-Scotland Overflow Water, DSOW - Denmark Strait Overflow Water, NADW - North Atlantic Deep Water, LDW - Lower Deep Water, and SAF - Subarctic Front.

Figure 2. Bathymetry of the CGFZ area according to Skolotnev *et al.* (2021b) and the location of the studied and referenced sediment cores (see Table 1). The major faults and rift axis positions are from Skolotnev *et al.* (2021b). Light-blue squares outline bathymetry charts in the corresponding figures. Note that core V53-C2 was collected 1 km southwest of the IODP site 1304. ITD - intra-transform domain, MAR - Mid-Atlantic Ridge.

Figure 3. Echo types of the CGFZ area.

Figure 4. Scheme of echo type and sedimentary facies distribution with a bathymetry background. The echo type descriptions are given in Figure 3. Pie charts show presence of sedimentary facies in the studied and referenced sediment cores. Blue arrows show the propagation of the Iceland-Scotland Overflow Water (ISOW) current. White and dark grey isobaths correspond to 1,500 m and 3,500 m depths, which are the upper and lower boundaries of the ISOW. ITD - intra-transform domain, MAR - Mid-Atlantic Ridge.

Figure 5. Scheme of echo type distributions (a), examples of cross-valley bathymetric profiles (b, c, and f), high-resolution seismo-acoustic profiles (d and e), and archive low-resolution seismic profile (g) for the northern and southern valleys of the eastern sector of the CGFZ. The position of (a–g) profiles is shown in (a). Grey lines on the bathymetric chart denote the position of the channel-like structures in the northern valley. The Iceland-Scotland Overflow Water (ISOW) near-bottom current is shown by blue arrows in (a) and blue circles in (b–g). The colour schemes for the bathymetry are the same as in Figure 2. The echo type descriptions are in Figure 3. White and dark grey isobaths on (a) are 1,500 m and 3,500 m depths, respectively. 1 – intra-transform spreading centre, ITD – intra-transform domain, MAR – Mid-Atlantic Ridge, U1 – upper acoustically semitransparent seismic unit.

Figure 6. Scheme of echo type distributions (a), examples of high-resolution seismo-acoustic profiles (b and d–h), and archive low-resolution seismic profile (c) for the northern and southern valleys of the western sector of the CGFZ. The location of sediment cores is shown on the sub-bottom profiles by arrows; the position of the sediment core KS 7911 (Faugères *et al.* 1983) is projected onto the sub-bottom profile (f). The colour schemes for the bathymetry are the same as in Figure 2. The echo type descriptions are in Figure 3. White and dark grey isobaths on (a) are 1,500 m and 3,500 m depths, respectively. 1 – intra-transform spreading centre, 2 – oceanic core complex, ITD – intra-transform domain, M – median ridge, T – terrace, U1 – upper acoustically semitransparent seismic unit.

Figure 7. Scheme of echo type distributions (a), high-resolution sub-bottom profiles (b), and bathymetric profile (c) of the sediment drift on the eastern flank of the Reykjanes Ridge. The direction of the Iceland-Scotland Overflow Water (ISOW) flow is shown by blue arrows. The location of core V53-C2 and IODP site 1304 (Channell *et al.* 2006) is shown by arrows on (b). The colour schemes for the bathymetry are the same as in Figure 2. The echo type descriptions are in Figure 3.

White and dark grey isobaths on (a) are 1,500 m and 3,500 m depths, respectively. U1 – upper acoustically semitransparent seismic unit.

Figure 8. Sedimentary logs for core V53-C1, collected in the northern active valley of the CGFZ. Red stars indicate  $^{14}\text{C}$  dates with cal ka BP denoted beneath each star. IRD – ice-rafted debris, MS – magnetic susceptibility.

Figure 9. Sedimentary logs for core V53-C2, collected in the isolated depression on the eastern flank of the Reykjanes Ridge. Red stars indicate  $^{14}\text{C}$  dates with cal ka BP denoted beneath the star. Yellow star indicates an additional time point from the ash layer. IRD – ice-rafted debris, MS – magnetic susceptibility.

Figure 10. Grain-size composition, representative grain-size distributions, and bulk mineral content for cores V53-C1 (a) and V53-C2 (b). Amphibole content (relative %) for cores V53-C1, V53-C2, and HU91-045-080 (Fagel and Mattielli 2011) (c). Bulk mineral content for core HU91-045-080 is from Fagel and Mattielli (2011) (d). Dotted lines show the correlation of the well-dated HU91-045-080 core with the core V53-C2 by mineralogical composition. Black arrows indicate bi-gradational trends in the mineral subfraction of F1 facies and blue arrow shows normal grading trend in the F4 facies. Facies description is in Figure 8 and Figure 9.

Figure 11. Vertical facies associations, identified in the studied sediment cores with connection to the estimated hydrodynamic regime and intensity of sea-surface bioproductivity.

Figure 12. Correlation of the seismo-acoustic profiler records with the sediment cores from confined contourite drift on the flank of the Reykjanes Ridge (a) and plastered drift in the northern active valley (b). The cyclic alternation of acoustically transparent/semitransparent (T) and reflective (R) units is proposed to be associated with intercalation of contouritic and hemipelagic/pelagic deposition, respectively, linked to climate changes. Stratigraphy and depths of core 13JPC are redrawn from Hodell *et al.* (2010). The grey fill on the core diagrams, superimposed on the profiler, corresponds with glacial intervals (MIS 4–2) in the sediments. Facies numbers are described in Figure 8 and Figure 9. AZ1 – North Atlantic Ash Zone 1, U1 – upper acoustically semitransparent seismic unit.

Figure 13. Scheme of sedimentation processes in the CGFZ. Arrows indicate bottom currents of the Iceland-Scotland Overflow Water (ISOW) in light blue and the Lower Deep Water (LDW) and Denmark Strait Overflow Water (DSOW) in purple. The question mark near the abbreviation of water masses denotes uncertainty in their origin. ITD – intra-transform domain, MAR – Mid-Atlantic Ridge.

Figure 14. Late Quaternary changes of the deep and intermediate water circulation in the CGFZ area, corresponding with interglacial (a) and glacial (b) conditions in the North Atlantic Ocean. The water boundaries are compiled according to Sarthein *et al.* 1994; Rahmstorf 2002; Thornalley *et al.* 2010. The grey dotted line in (a) corresponds to 34.94 isohaline drawn according to Bower and Furey (2017) and outlined the modern boundaries of the Iceland-Scotland Overflow Water (ISOW). Red arrows denote the position of the studied sediment cores. GAABW – Glacial Antarctic Bottom Water, GNAIW – Glacial North Atlantic Intermediate Water, ITD – intra-transform domain, MAR – Mid-Atlantic Ridge.

### Table Captions

Table 1. Location of the sediment cores in the study area. Cores from the same location are shown in italics.

Table 2. Results of radiocarbon dating for V53-C1 and V53-C2 sediment cores. Radiocarbon ages were calibrated using Calib8.2 and MARINE20 calibration curve (Heaton *et al.* 2020) with the global ocean age ( $\Delta R$ ) of 550 years.

ACCEPTED MANUSCRIPT

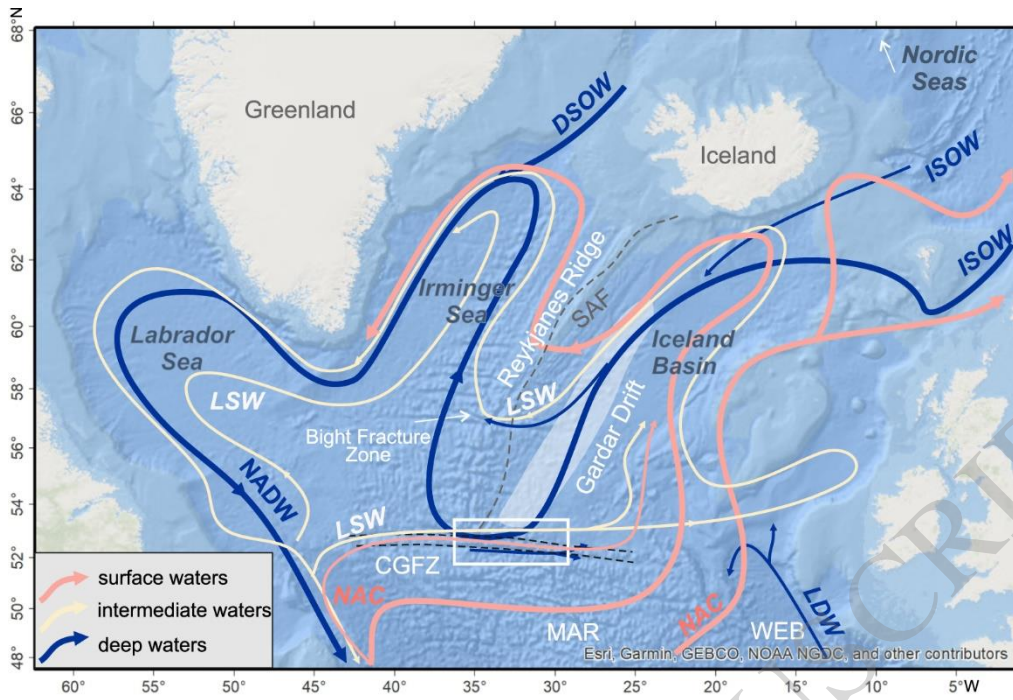
| Core                          | Lat. N            | Long. W           | Water depth (m) / length (m) | References                            |
|-------------------------------|-------------------|-------------------|------------------------------|---------------------------------------|
| V53-C1                        | 52°37.080'        | 33°34.726'        | 3850 / 4.65                  | This study                            |
| V53-C2                        | 53°03.301'        | 33°32.719'        | 3140 / 5.20                  | This study                            |
| <i>IODP1304</i>               | <i>53°03.401'</i> | <i>33°31.781'</i> | <i>3080 / 264</i>            | <i>Expedition 303 Scientists 2006</i> |
| <i>KN166-14-13JPC (13JPC)</i> | <i>53°03.410'</i> | <i>33°31.78'</i>  | <i>3082 / 12</i>             | <i>Hodell et al. 2010</i>             |
| <i>HU91-045-080</i>           | <i>53°03.40'</i>  | <i>33°31.78'</i>  | <i>3024 / 3.30</i>           | <i>Fagel and Mattielli 2011</i>       |
| AMK-4515                      | 52°03.14'         | 29°00.12'         | 3630 / 3.70                  | Bashirova <i>et al.</i> 2017          |
| KS 7701                       | 52°21.2'          | 35°10.4'          | 3780 / 5.40                  | Faugères <i>et al.</i> 1983           |
| KS 7910                       | 52°19.4'          | 35°38.4'          | 3790 / 9.70                  | Faugères <i>et al.</i> 1983           |
| KS 7911                       | 52°42.0'          | 35°27.5'          | 3650 / 10.7                  | Faugères <i>et al.</i> 1983           |
| KS 7912                       | 52°46.0'          | 35°27.6'          | 3460 / 2.38                  | Faugères <i>et al.</i> 1983           |

**Table 1**

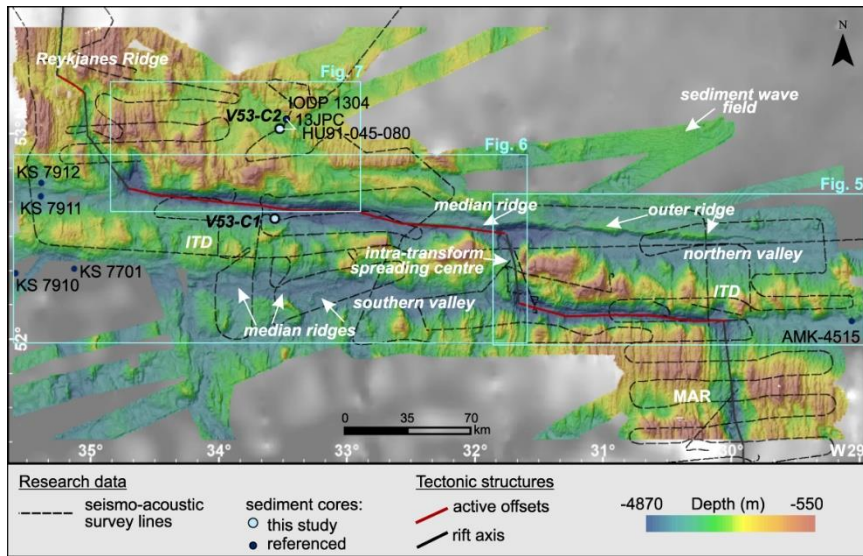
| Lab. code | Core name and depth (cm) | Dated material               | <sup>14</sup> C age (a BP) | Error ± | 1 sigma (cal a BP) | Calibrated age median (cal ka BP) |
|-----------|--------------------------|------------------------------|----------------------------|---------|--------------------|-----------------------------------|
| GV-4069   | V53-C1<br>0-1            | Bulk planktonic foraminifera | 882                        | 40      | 281-423            | 0.35                              |
| GV-4070   | V53-C1<br>160-161        | Bulk planktonic foraminifera | 8223                       | 47      | 8428-8607          | 8.53                              |
| GV-4071   | V53-C2<br>320-321        | Bulk planktonic foraminifera | 10224                      | 52      | 11093-11256        | 11.18                             |

**Table 2**

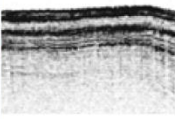
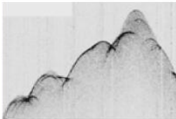
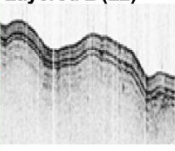
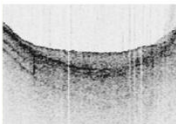
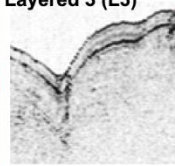

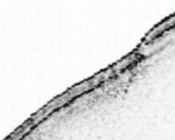
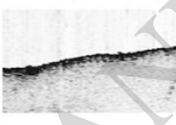
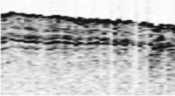
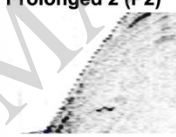
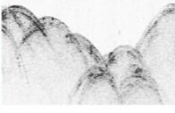
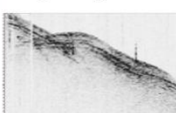







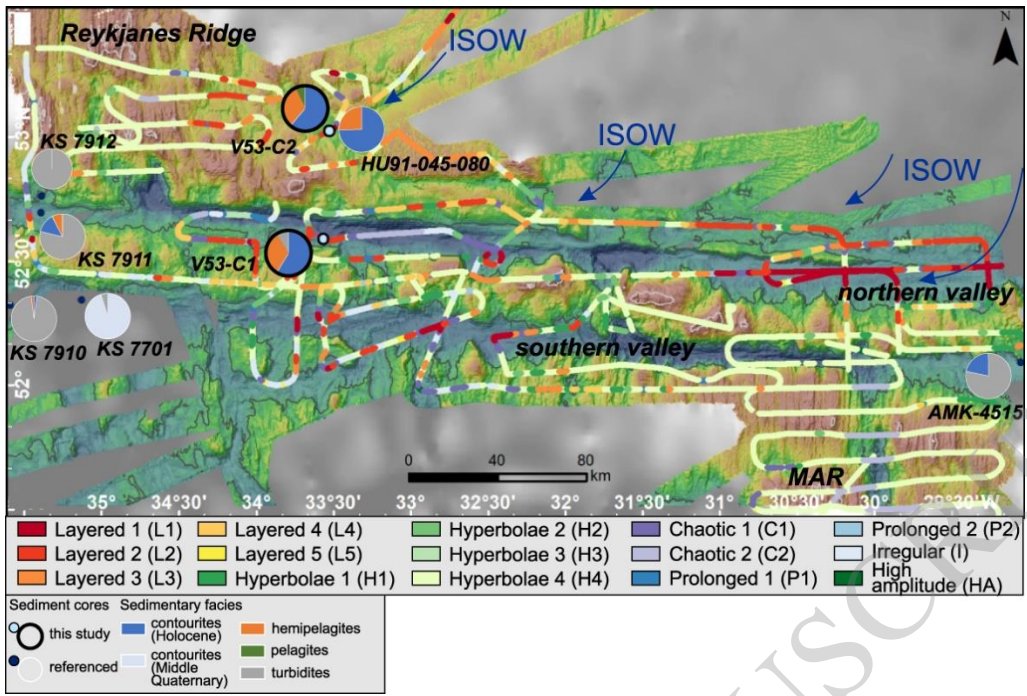
**Figure 1**



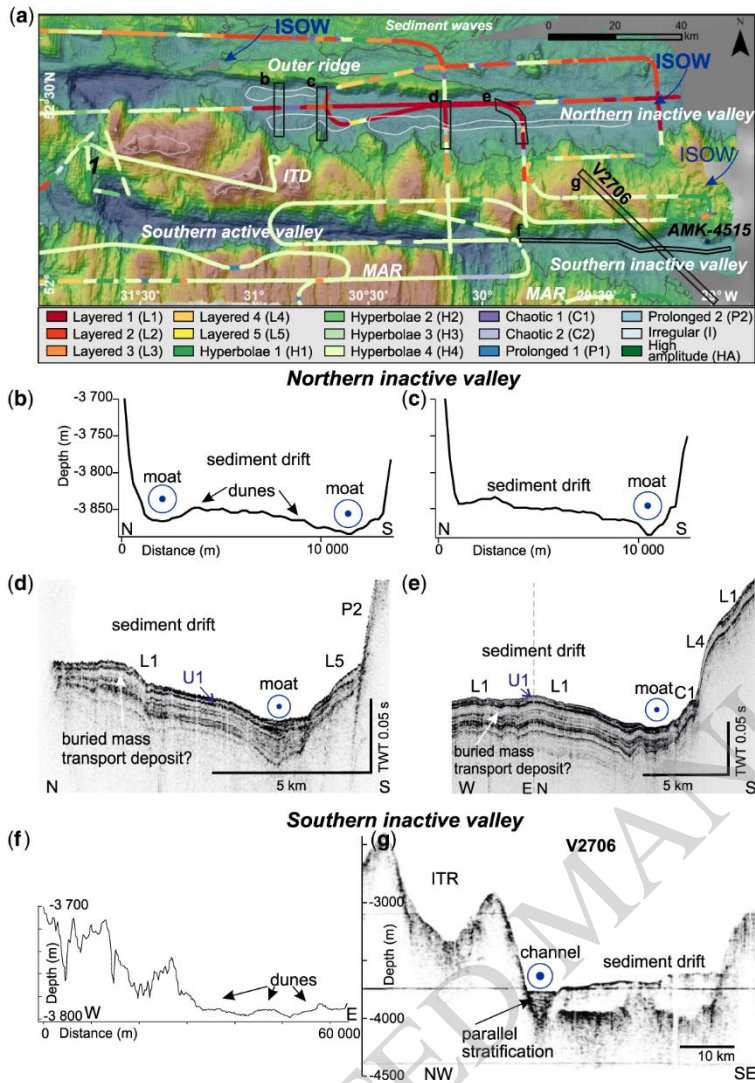
**Figure 2**

|    | Echo type   | Description  | Interpretation                                       |    | Echo type   | Description  | Interpretation   |
|----|---|--|--|----|---|--|--|
| L1 | <b>Layered 1 (L1)</b><br>      | Flat surface with package of high-amplitude continuous parallel reflectors                                   | Mixed deposition: hemipelagic and by bottom currents | H4 | <b>Hyperbolae 4 (H4)</b><br>     | Singular, large, irregular hyperbolic echoes without sub-bottom reflectors   | High-angle slopes and ridges without sediment cover          |
| L2 | <b>Layered 2 (L2)</b><br>      | Undulating continuous surface reflector underlain by well-stratified conformable reflectors                  | Mixed deposition: hemipelagic and by bottom currents | C1 | <b>Chaotic 1 (C1)</b><br>        | Transparent lens-shaped echo, sometimes with chaotic filling underneath prolonged flat or undulating surface reflector | Mass-transport and gravity flows deposits                    |
| L3 | <b>Layered 3 (L3)</b><br>      | Undulating high-amplitude surface reflector with one sharp conformable underlying reflector                  | Mixed deposition: hemipelagic and by bottom currents | C2 | <b>Chaotic 2 (C2)</b><br>        | Reflection with almost complete mask of acoustic inner stratification by turbidity pattern                             | Mass-transport and gravity flows deposits                    |
| L4 | <b>Layered 4 (L4)</b><br>      | Flat or slightly undulating high-amplitude surface reflector with one sharp conformable underlying reflector | Pelagic or hemipelagic sedimentation                 | P1 | <b>Prolonged 1 (P1)</b><br>     | Distinct prolonged reflection. Sub-bottom reflectors are scarce or absent  | Low-angle slopes with limited or without sediment cover      |
| L5 | <b>Layered 5 (L5)</b><br>    | High-amplitude compacted stratified and discontinuous reflectors   | Deposition in contourite channel                     | P2 | <b>Prolonged 2 (P2)</b><br>    | Distinct prolonged bottom surface reflectors with low amplitude irregular sub-bottoms                                  | Slopes without sediment cover                                |
| H1 | <b>Hyperbolae 1 (H1)</b><br> | Hyperbolae of different height with conformable or irregular sub-bottoms.                                    | Hemipelagic or deposition by bottom currents         | I  | <b>Irregular (I)</b><br>       | Irregular undulating surface with rare irregular and discontinuous sub-bottoms   | Low-angle slopes or ridge summit with limited sediment cover |
| H2 | <b>Hyperbolae 2 (H2)</b><br> | Repeating hyperbolae with vertices tangent to the seafloor or a sub-bottom reflectors                        | Low-angle slopes without or with thin sediment cover | HA | <b>High amplitude (HA)</b><br> | High-amplitude surface and internal reflectors   | Volcanic material  |
| H3 | <b>Hyperbolae 3 (H3)</b><br> | Low-amplitude irregular hyperbolae of different vertex high with unconformable hyperbolae sub-bottoms        | Erosional channels                                   |    |   |  |  |

**Figure 3**



**Figure 4**



**Figure 5**

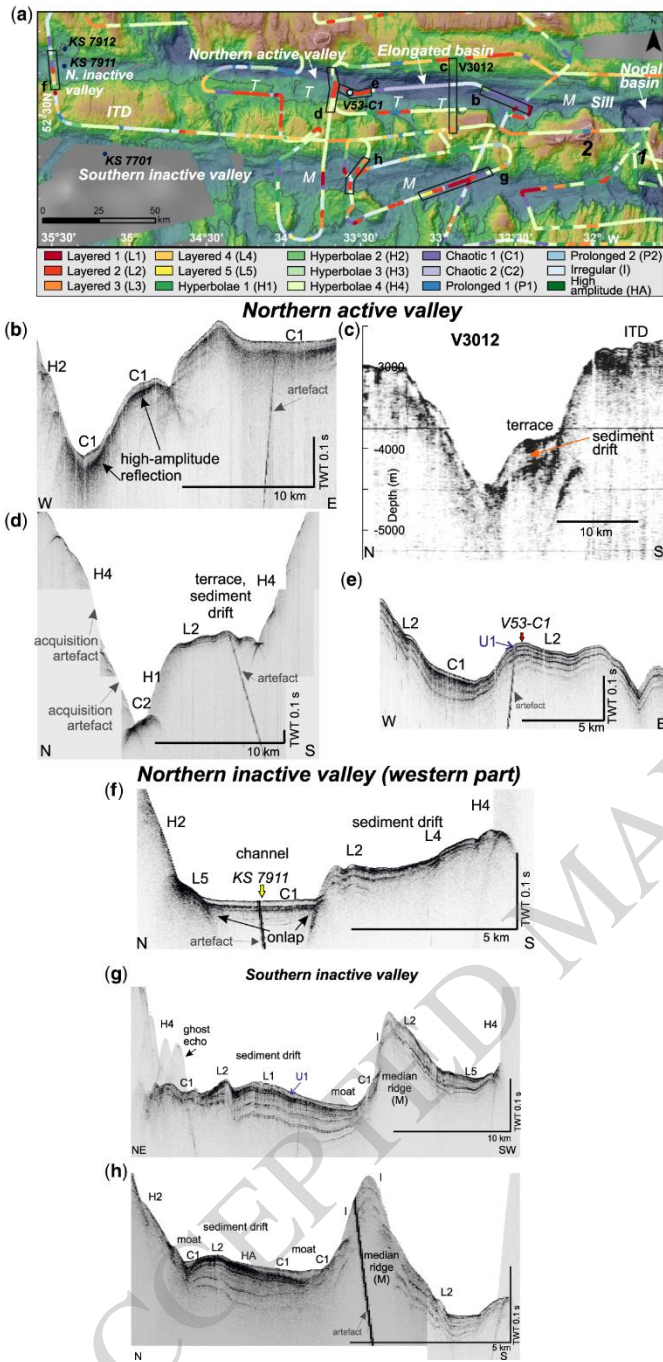
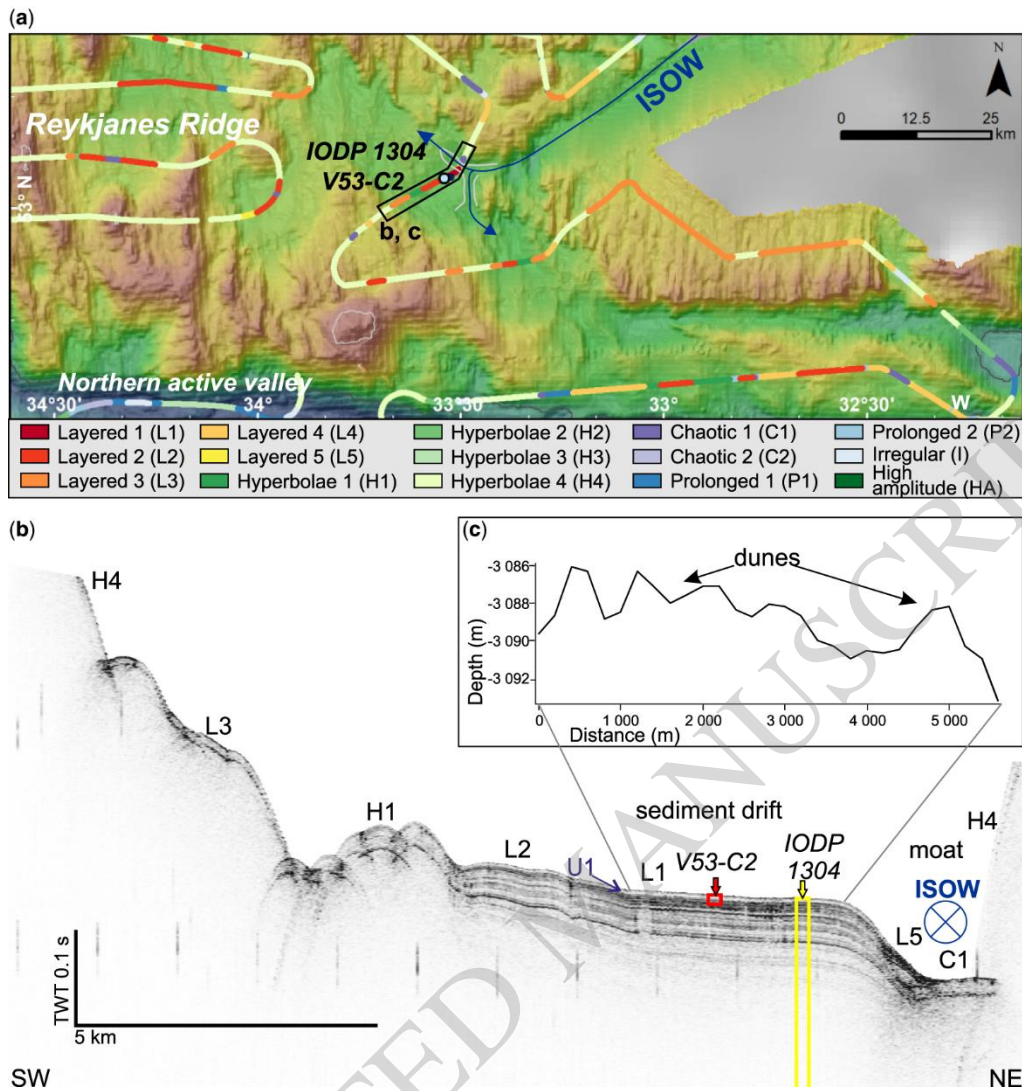


Figure 6



**Figure 7**

V53-C1 (northern active valley, 3851 m depth)

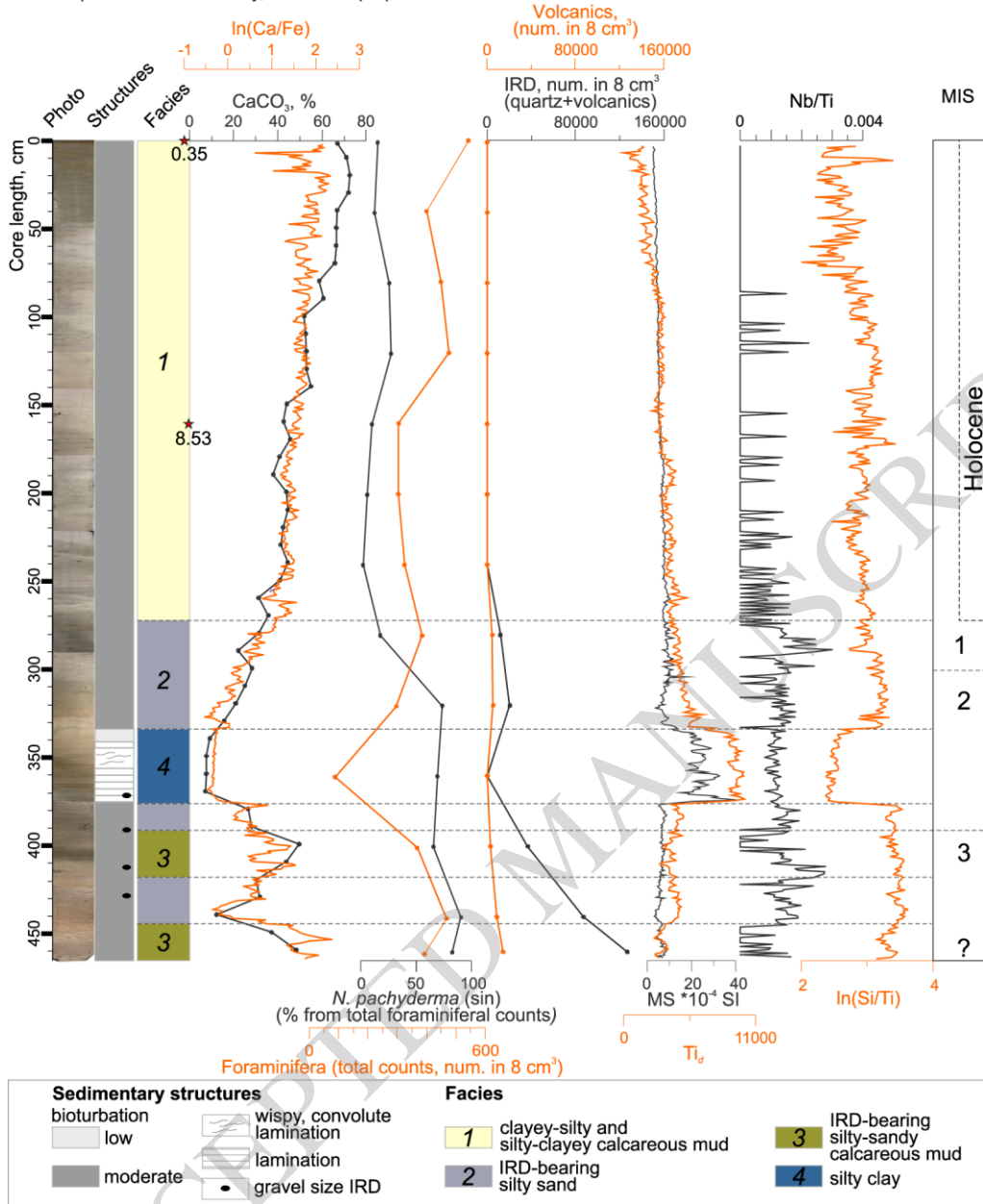


Figure 8



V53-C2 (flank of the Reykjanes Ridge, 3138 m depth)

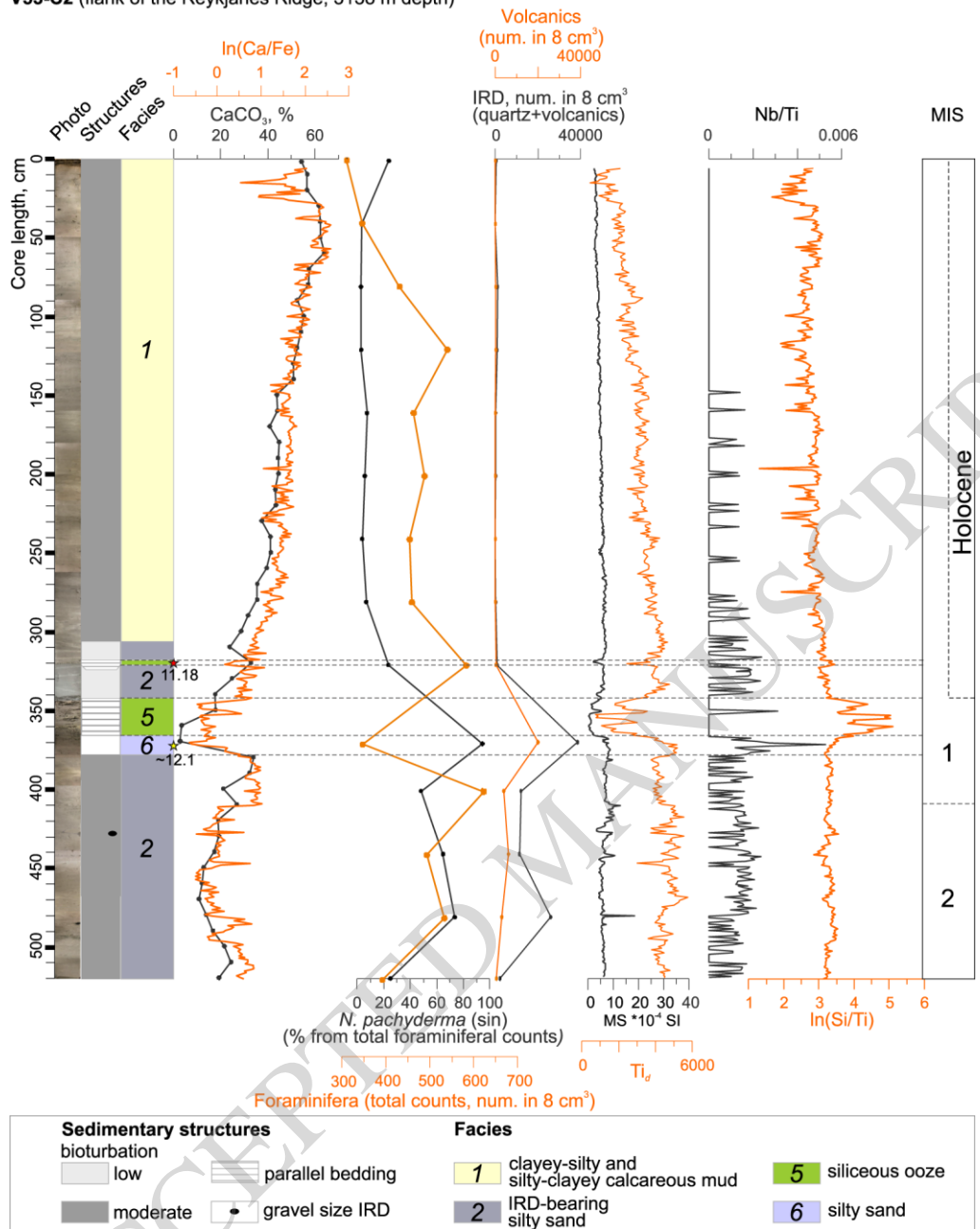
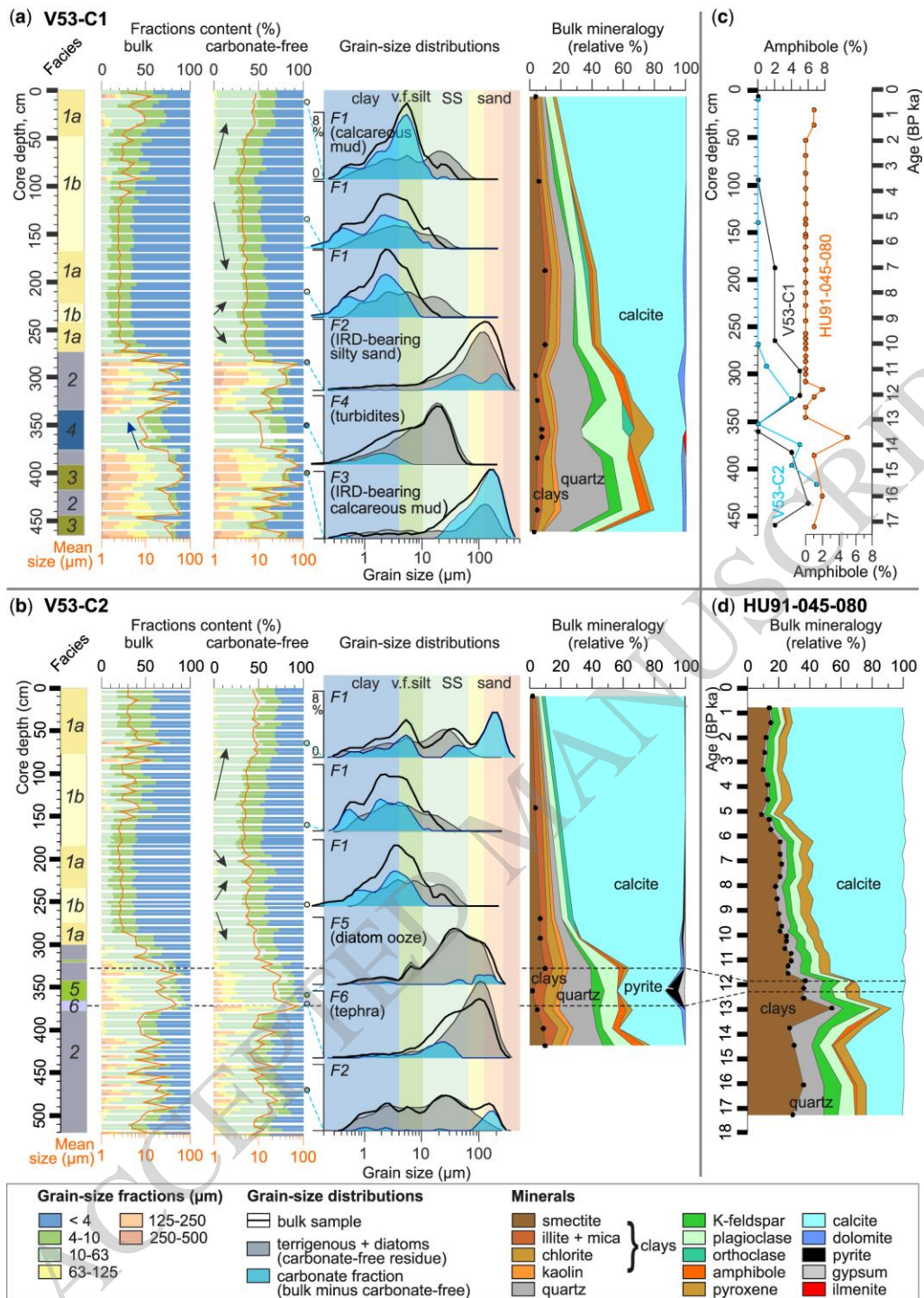


Figure 9



**Figure 10**

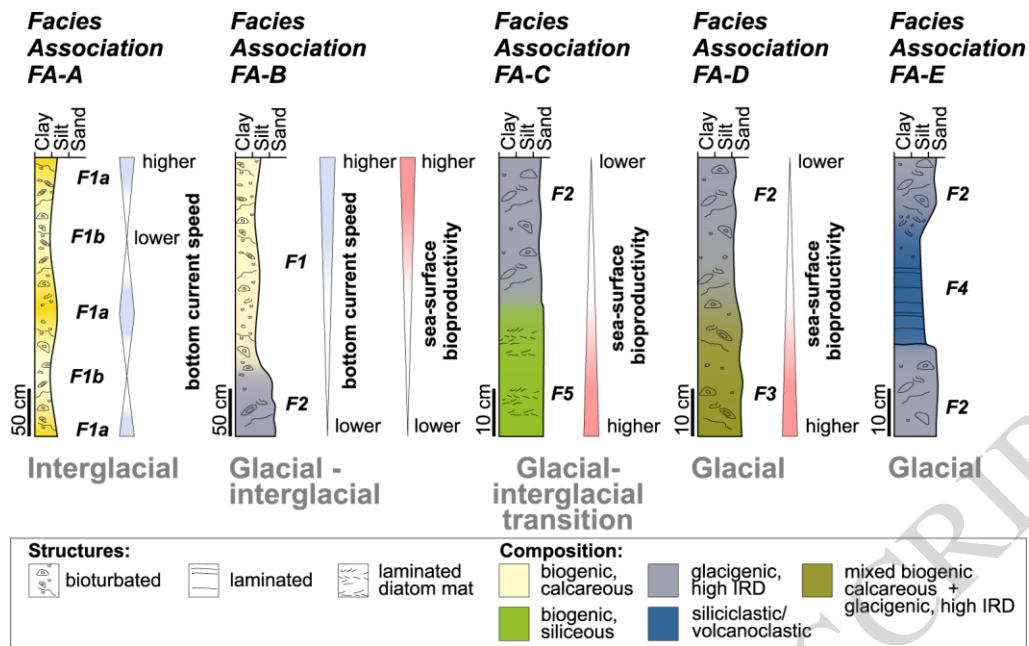
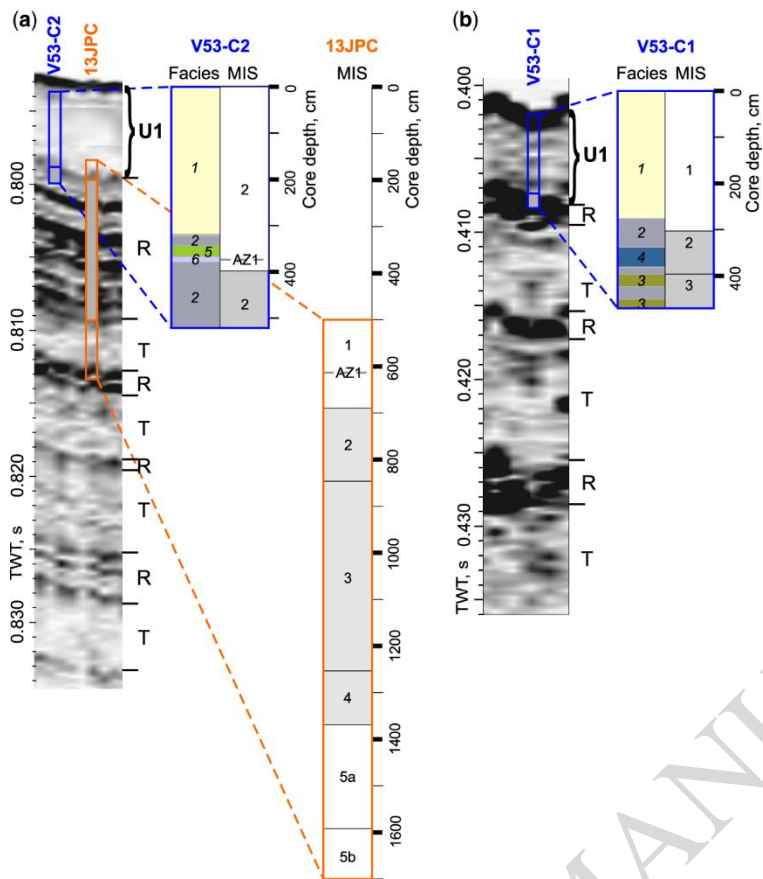
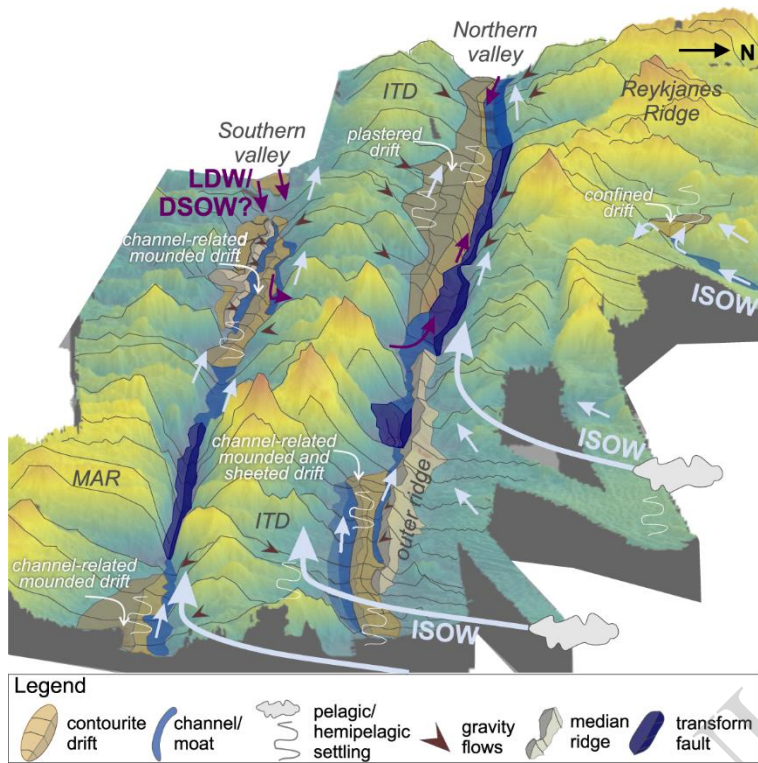


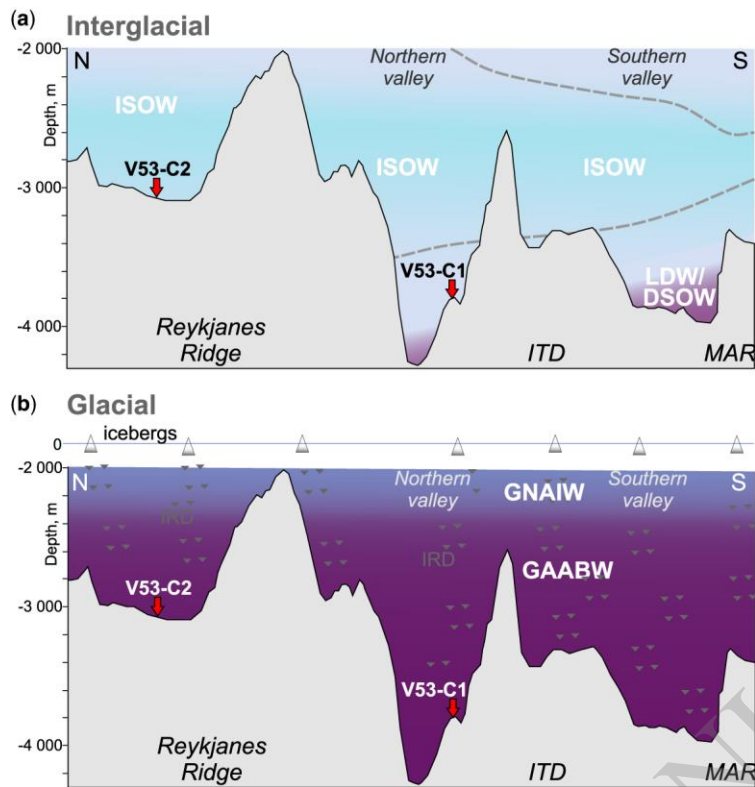
Figure 11



**Figure 12**



**Figure 13**



**Figure 14**